Modelling of GPR Wave Propagation and Scattering in Inhomogeneous Media

Karsten Müller

Master Thesis in Geosciences

Petroleum Geology and Geophysics

Department of Geosciences
University of Oslo

Spring 2005

Abstract

Numerical modelling of GPR wave propagation is becoming more and more important. The ability to build complex models to mirror complex subsurface structures can improve our understanding of how electromagnetic waves are effected by it.
The main task of this thesis was to develop a model generator which simplifies complex model building by applying statistical processes. Both, the distribution of inhomogeneities and random rough surfaces can be described statistically.
The developed model builder *modelGPR* uses Gaussian distribution to create rough surfaces and to embed inhomogeneities into a host medium.
The potentials of the software are presented by two examples. The first is related to ground truth measurements for SAR-satellites in polar regions and the second is devoted to water detection in the Martian shallow subsurface.

For my parents Doris and Hans-Peter

Contents

Chapter 1

Introduction

Commercially available GPR modelling software like REFLEXW has a built in model generator tool. This model software can make simple deterministic shapes like smooth interfaces, blocks and spheres. These models work well when the radar wavelength is shorter than the reflecting object or longer than the interface roughness at the reflecting interface. If the subsurface medium has inhomogeneities or interface surface roughness with a size comparable to the radar wavelength scattering occurs.
The consideration of all different types of surfaces and subsurface inhomogeneities is practically impossible [Kozlov et al., 2001]. Therefore the modelling of statistically described subsurface environments and interfaces (e.g. surfaces with arbitrary degree of roughness) is necessary.
The intention of my thesis is to program a model generator which can create multi rough-layered models with statistically distributed inhomogeneities. The generated model should serve as an input file for the finite-difference time-domain (FD-TD) software *GprMax* in order to receive the radar response signal of the modelled subsurface.
Two example applications should illustrate the use and capability of my program *modelGPR*. The first example models 5.3 GHz GPR scattering from glaciers on Svalbard to support ground truth measurements for SAR-satellites. In line with the *Envitools*

project [Guneriussen et al., 2002] an intense study of the glaciers Kongsvegen and Holtedahlfonna is accomplished, combining synthetic aperture radar (SAR), ground-penetrating radar (GPR) and glaciological data sets. The model should give an idea which layers and structures in the near-surface region of the glaciers contribute to the backscatter received by the SAR.

A field of current interest is the modelling of electromagnetic wave propagation in Martian soil. Several missions, to investigate the subsurface of Mars have been flown, and more will be launched in the near future. Radar system evaluation for these missions is strongly dependent on a wide variety of models, considering various possible conditions [Leuschen et al., 2003]. With regard to the *WISDOM* project [Berthelier and Hamran, 2003] a 2-D model will be introduced to study attenuation and scattering of Martian soil.

The remaining part of the introduction is a guide through the basics of electromagnetic wave propagation and radar surveys. Chapter 2 will present the FD-TD method and common GPR modelling tools. The Statistical Modelling chapter (Chapter 3) deals with the discretisation of subsurface geometry and its statistics. It closes with a description of the algorithms used in *modelGPR*. Chapters 4 and 5 contain the example applications of *modelGPR*.

For further reading on the subject *GPR* and *Remote Sensing* I recommend the books of Daniels [Daniels, 2004] and Ulaby [Ulaby et al., 1982].

1.1 Radar surveys

Ground-penetrating radar detects dielectric discontinuities and hence makes it possible to investigate objects that are buried in visually opaque media (Figure 1.1). This includes interfaces and three-dimensional objects of nearly any size and shape, if the appropriate frequency is chosen.

Penetration distances from a couple of centimeters with high frequencies (high res-

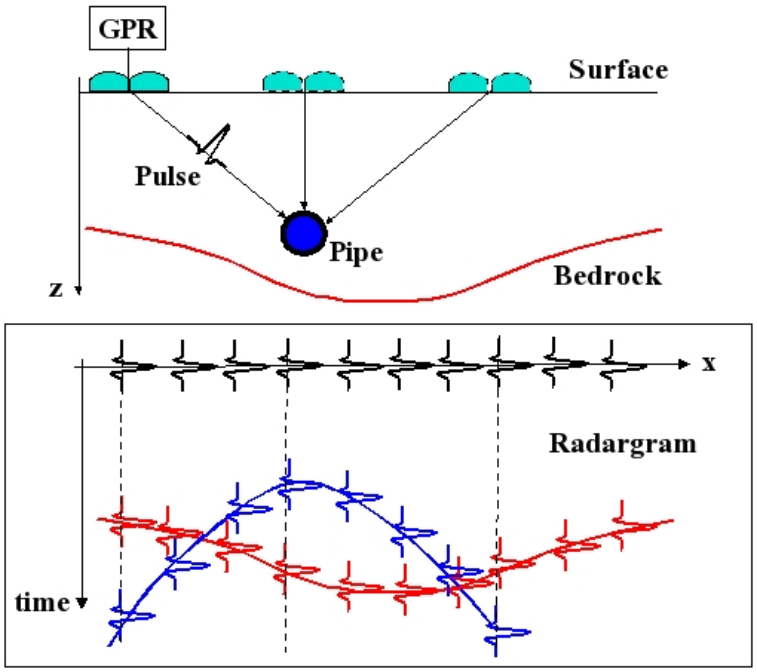

Figure 1.1: *The figure illustrates a general GPR survey. The antenna couple is dragged along the surface, while the transmitter emits pulses. These are partly reflected at interfaces and buried objects and recorded at the receiver. The signal is displayed in a radargram where the received pulses are arranged with regard to their arrival time, assuming a zero-offset experiment. Horizontal layers appear as true images in the radargram (red), cylindrical, spherical and point scatterers result in a diffraction hyperbola (blue). [Figure taken from lecture notes by S.E. Hamran]*

olution) up to several kilometers at very low frequencies (poor resolution) can be achieved. The signal attenuation at the desired operating frequency in a given medium is the main factor that limits the penetration depth. High frequencies are more strongly attenuated than low frequencies, resulting in poorer resolution with depth. GPR is mainly deployed in two basic modes: a) reflection surveys and b) velocity analysis (Figure 1.2). The goal of a reflection survey is to identify structures in visually opaque materials without changing or even destroying it. Transmitter and receiver are often closely spaced in this mode and are moved in constant intervals, ideally smaller than the potential target. In this manner large profiles or areas can be investigated at a low expense of time.

The velocity analysis often supports reflection surveys by giving an approximation of

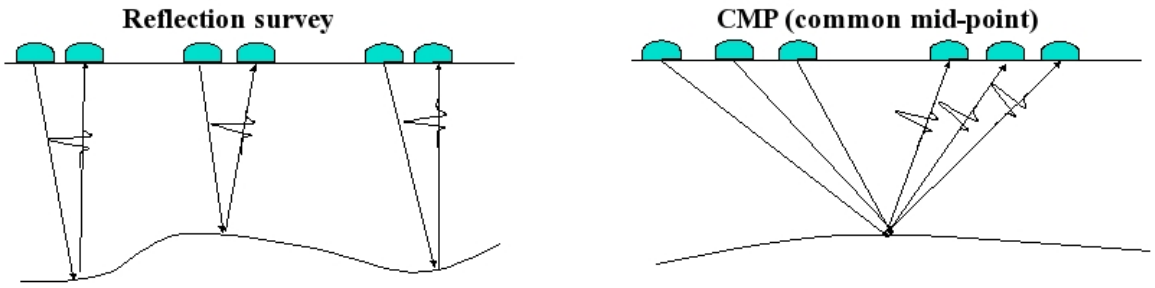

Figure 1.2: *The two basic GPR survey geometries: Reflection survey and velocity analysis in CMP mode. [Figure taken from lecture notes by S.E. Hamran]*

the medium velocities. It is usually applied in the common midpoint (CMP) mode, where transmitter and receiver are moved equidistant from a common midpoint leading to progressively deeper penetration and reflection from deeper structures. In horizontally layered media the exact medium velocities can be obtained iteratively from top to bottom by picking the arrival times of the refracted waves. For arbitrary orientated layers only an approximation of the velocities is possible.

GPR's ability to use remote, non-contacting transducers to radiate energy, rather than the ground-contacting types needed for seismic investigations, makes it a fast and suitable application to map remote areas from air or space [Daniels, 2004]. Surface-penetrating radar has found its way into many different sectors like civil-engineering, medical-imaging, remote sensing, geophysical investigations and many more.

The signal received by the antenna is the portion of the incident energy that is scattered back at interfaces and objects and yields information about them. The fundamental relation between the characteristics of the radar, the target, and the received signal is given by the *radar equation* [Ulaby et al., 1982]

$$P_r = \frac{P_t G_t A_r}{(4\pi)^2 R_t^2 R_r^2}\sigma, \tag{1.1.1}$$

where P_r and P_t are the received and transmitted power, G_t is the antenna gain, A_r the effective receiving area (receiver antenna aperture), R_r and R_t are the ranges between target and receiver and target and transmitter and σ is the scattering cross-section (radar cross-section). The cross-section σ is a function of the directions of

the incident wave and the wave reflected or scattered towards the receiver, as well as the scatterer's shape and dielectric properties [Ulaby et al., 1982]. The average value of the scattering cross-section per unit area is defined as the dimensionless scattering coefficient σ^0:

$$\sigma^0 = \langle \frac{\sigma}{\Delta A} \rangle \tag{1.1.2}$$

In microwave remote sensing the parameter of interest is generally the *backscattering coefficient*. For a mono-static radar (transmitter and receiver at the same location) R_r and R_t are the same and the scattering coefficient is then called the backscattering coefficient, because only the energy scattered directly back towards the antenna is received. It is common to express the backscattering coefficient in Decibels (dB), because it can vary over two or three orders of magnitude.

1.2 Propagation of electromagnetic waves in dielectric materials

Electromagnetic wave propagation is fully described by Maxwell's equations (here in differential form):

$$\nabla \times \vec{E} = -\frac{\partial \vec{B}}{\partial t} - \vec{J}_m \tag{1.2.1}$$

$$\nabla \times \vec{H} = \frac{\partial \vec{D}}{\partial t} + \vec{J}_e \tag{1.2.2}$$

$$\nabla \cdot \vec{B} = 0 \tag{1.2.3}$$

$$\nabla \cdot \vec{D} = q_v \tag{1.2.4}$$

with the following parameters:

$\vec{E}\hat{=}$ electric field $[Vm^{-1}]$

$\vec{H}\hat{=}$ magnetic field $[Am^{-1}]$

$\vec{D}\hat{=}$ electric flux $[Cm^{-2}]$

$\vec{B}\hat{=}$ magnetic flux $[Wbm^{-2}]$

$\vec{J_e}\hat{=}$ electric current density $[Am^{-2}]$

$\vec{J_m}\hat{=}$ magnetic current density $[Vm^{-2}]$

$q_v\hat{=}$ electric charge density $[Cm^{-3}]$

$t\hat{=}$ time $[s]$

They describe the relation between the electric and the magnetic field (Figure 1.3), which induce each other and are always perpendicular. Hence, Maxwell's equations are coupled and can only be uncoupled at the expense of raising their order. This leads to an uncoupled second-order partial differential equation, usually referred to as the wave equation [Balanis, 1989].

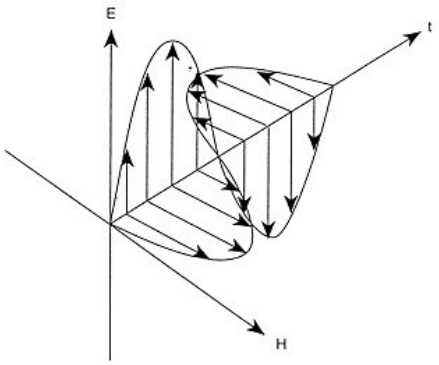

Figure 1.3: *Propagation of electromagnetic waves in free space [Daniels, 2004]*

The one-dimensional wave equation represents electromagnetic wave propagation in one direction, here the z-axis,

$$\frac{\partial^2 E}{\partial z^2} = \mu\epsilon\frac{\partial^2 E}{\partial t^2}. \tag{1.2.5}$$

In free space, an electromagnetic wave travels at the speed of light

$$c = \frac{1}{\sqrt{\mu_0 \epsilon_0}} = 299,792,458 ms^{-1}, \tag{1.2.6}$$

where $\mu_0 = 4\pi \cdot 10^{-7} T^2 m^3 J^{-1}$ is the permeability of free space and $\epsilon_0 = 8,854 \cdot 10^{-12} C^2 J^{-1} m^{-1}$ is the permittivity of free space. The propagation velocity within a dielectric material is

$$\nu = \frac{c}{\sqrt{\mu_r \epsilon_r}} \tag{1.2.7}$$

with the non-dimensional, relative permeability μ_r and permittivity ϵ_r of the material. The wavelength λ is defined as the distance the wave propagates in one period of oscillation and is the ratio between the medium velocity ν and the frequency f.

1.3 Surface- and volume-scattering

When an electromagnetic wave impinges on the interface between two media with different dielectric properties, a portion of its energy is scattered back and the rest is transmitted into the lower medium. The directions of the incident, reflected and transmitted wave are related to each other by Snell's Law

$$\frac{\sin \theta_i}{v_i} = \frac{\sin \theta_r}{v_r} = \frac{\sin \theta_t}{v_t}, \tag{1.3.1}$$

where θ_i is the incident angle, θ_r and θ_t the angle of reflection and transmission and $v_{i,r,t}$ are the corresponding medium velocities. Considering the lower medium as homogeneous, scattering is only influenced by the surface boundary. Hence, it is referred to as *surface-scattering*. In theory, the radiation pattern of a perfectly smooth (specular) surface is a delta function in the specular direction. In reality it consists of a large coherent and a small diffuse component (Figure 1.4a). With increasing surface roughness the radiation pattern becomes more and more diffuse and backscattering increases (Figure 1.4b-c).

The more realistic situation of an inhomogeneous medium composed of materials

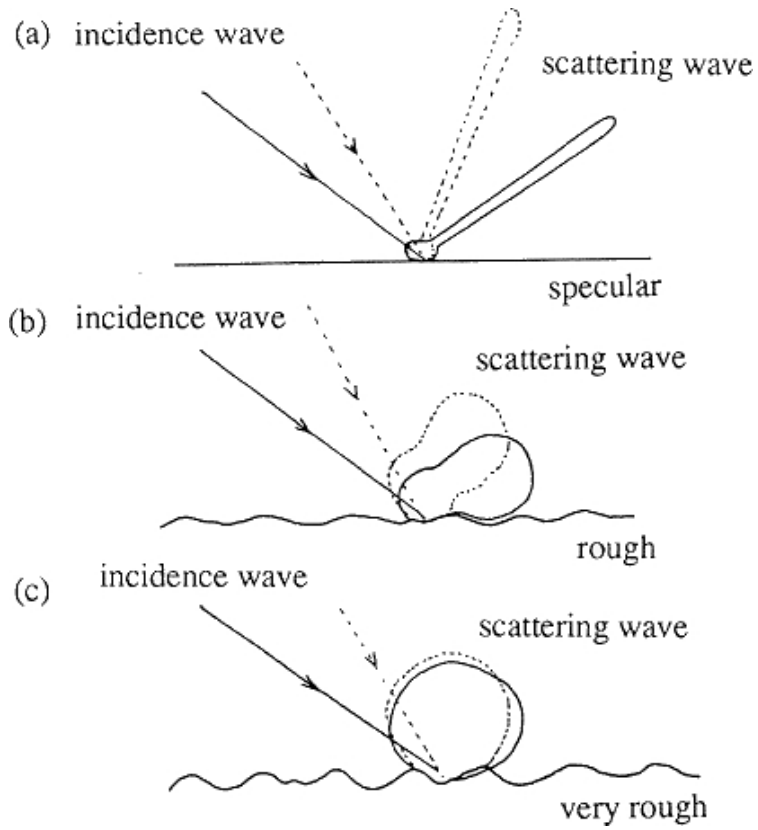

Figure 1.4: *Surface scattering patterns with different surface roughness. [Figure taken from* http://www.profc.udec.cl/~gabriel/tutoriales/rsnote/cp3/3-4-1.gif*]*

of different dielectric properties adds another component to the scattered portion. Part of the transmitted energy is scattered at the inhomogeneities and may cross the boundary to the upper medium. Because the scattering takes place in the medium, it is called *volume-scattering* (Figure 1.5). Scattering due to scatterers further away from the source is weaker due to the larger extinction (total loss).

In general volume-scattering is weaker than surface-scattering, because it causes a redistribution of energy in the transmitted wave in multiple directions, which results in a loss of energy. The total loss an electromagnetic waves experiences in a physical medium is the sum of the scattering loss and the loss due to conduction [Ulaby et al., 1982].

Scattering losses at an interface are governed by the intrinsic impedances η of the

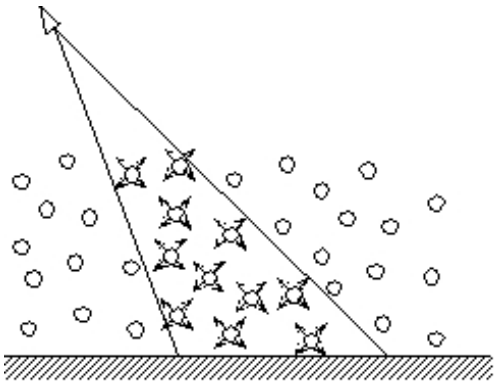

Figure 1.5: *Volume scattering at particles in a medium.*

upper and lower medium. The intrinsic impedance is the relationship between the electric field E and the magnetic field H in the medium

$$\eta = \frac{E}{H} = \sqrt{\frac{\mu}{\epsilon}}. \tag{1.3.2}$$

It is directly related to the reflectivity at normal incident on the boundary between two materials

$$r = \frac{\eta_2 - \eta_1}{\eta_2 + \eta_1}. \tag{1.3.3}$$

Conductive losses are dependent on the frequency of the electromagnetic wave, the relative permittivity and permeability and the loss tangent of the material

$$\tan\delta \approx \frac{\sigma}{\omega\epsilon}, \tag{1.3.4}$$

with the conductivity σ, the angular frequency ω and the permittivity ϵ. The conductivities of materials range over several orders of magnitude, from conductors with high conductivities to insulators. Natural soil and other materials that GPR observations are normally concerned with, lie in a range of $10^{-8} - 10^{2}$ S/m and belong to the insulator or semi-conductor class [Balanis, 1989].

Chapter 2

FD-TD Modelling and Present Model Generators

2.1 Basics of GPR modelling with the Finite-Difference Time-Domain method

Maxwell's equations 1.2.1-1.2.4 are first order partial differential equations (PDE) in which the field vectors are assumed to be single-valued, bounded, continuous functions of position and time [Balanis, 1989]. In order to model the waves propagation numerically, these equations have to be solved in a discretized area or volume.
The finite-difference time-domain (FD-TD) method, first introduced by Kane Yee [Yee, 1966] in 1966, offers a direct solution for Maxwell's time-dependent curl equations 1.2.1 and 1.2.2. Definition of the electric current density to account for the electric loss mechanisms and an equivalent magnetic current density for the magnetic loss mechanisms

$$\vec{J}_e = \sigma \vec{E} \tag{2.1.1}$$

$$\vec{J}_m = \rho' \vec{H} \tag{2.1.2}$$

and their substitution into the curl equations yields

$$\frac{\partial \vec{H}}{\partial t} = -\frac{1}{\mu}\nabla \times \vec{E} - \frac{\rho'}{\mu}\vec{H} \tag{2.1.3}$$

$$\frac{\partial \vec{E}}{\partial t} = \frac{1}{\epsilon}\nabla \times \vec{H} - \frac{\sigma}{\epsilon}\vec{E}, \tag{2.1.4}$$

where ϵ is the dielectric permittivity, σ the electrical conductivity, μ the magnetic permeability and ρ' is the magnetic resistivity [Taflove and Hagness, 2000].
The system of these six coupled PDEs forms the basis of the FD-TD numerical algorithm for electromagnetic wave interactions with general 3-D-objects
[Taflove and Hagness, 2000, Yee, 1966]. A short introduction will be given to the FD-TD method for the two dimensional case.
Assuming that in a Cartesian coordinate system (x,y,z) neither the electromagnetic field excitation nor the modelled geometry will have any variation in the z-direction, all partial derivatives with respect to z in equations 2.1.3 and 2.1.4 will be zero, yielding

$$\frac{\partial H_x}{\partial t} = \frac{1}{\mu}\left(-\frac{\partial E_z}{\partial y} - \rho' H_x\right) \tag{2.1.5}$$

$$\frac{\partial H_y}{\partial t} = \frac{1}{\mu}\left(\frac{\partial E_z}{\partial x} - \rho' H_y\right) \tag{2.1.6}$$

$$\frac{\partial E_z}{\partial t} = \frac{1}{\epsilon}\left(\frac{\partial H_y}{\partial x} - \frac{\partial H_x}{\partial y} - \sigma E_z\right) \tag{2.1.7}$$

$$\frac{\partial E_x}{\partial t} = \frac{1}{\epsilon}\left(\frac{\partial H_z}{\partial y} - \sigma E_x\right) \tag{2.1.8}$$

$$\frac{\partial E_y}{\partial t} = \frac{1}{\epsilon}\left(-\frac{\partial H_z}{\partial x} - \sigma E_y\right) \tag{2.1.9}$$

$$\frac{\partial H_z}{\partial t} = \frac{1}{\mu}\left(\frac{\partial E_x}{\partial y} - \frac{\partial E_y}{\partial x} - \rho' H_z\right). \tag{2.1.10}$$

Equations 2.1.5-2.1.7 and 2.1.8-2.1.10 are now decoupled PDEs reflecting, respectively, the transverse magnetic (TM) mode and the transverse electric (TE) mode in two dimensions.

2.1.1 The Yee algorithm

Yee's algorithm solves the electric and magnetic field in time and space in a coupled manner using Maxwell's curl equations 2.1.3 and 2.1.4. The partial differential equations Yee used are centered finite-difference expressions for the space and time derivatives of second order accuracy in space and time increments. In the Yee space lattice each $\vec{E}$ component is surrounded by four $\vec{H}$ components and vise versa. The distance between the single components of the electric or magnetic field are given by Δx, Δy and Δz for simplicity called Δ from now on assuming that $\Delta x = \Delta y = \Delta z$. The $\vec{E}$ and $\vec{H}$ components are arranged in time in *leapfrog* fashion. In this manner the electric and magnetic field are calculated one after another at an interval of $\Delta t/2$, thereby avoiding simultaneous equations.
The notation for a function of space and time is

$$f(i\Delta x, j\Delta y, k\Delta z, n\Delta t) = f^n_{i,j,k}, \tag{2.1.11}$$

where i,j,k and n are integers defining the progression in the directions x,y,z and in time t. We apply this notation to equation 2.1.5 as an example.

$$\frac{H^{n+\frac{1}{2}}_{x;i,j,k} - H^{n-\frac{1}{2}}_{x;i,j,k}}{\Delta t} = \frac{1}{\mu_{i,j,k}} \left(- \frac{E^n_{z;i,j+\frac{1}{2},k} - E^n_{z;i,j-\frac{1}{2},k}}{\Delta y} - \rho'_{i,j,k} H^n_{x;i,j,k} \right) \tag{2.1.12}$$

The choice of Δ and Δt effects the solution of the PDEs and can lead to numerical instability. In order to avoid an uncontrolled increase of the computed value with time, the time step Δt must be bounded. The relation between Δ and Δt results from an eigenvalue problem. The upper bound for Δt is Δ/c, where c is the propagation velocity.

2.1.2 Absorbing boundary conditions

A major difference between computational models and the real subsurface is the limitation of the model in space due to the fact that no computer can store unlimited

data.

If the time window for the calculation is larger than the time an electromagnetic wave needs to travel to the boundary of the model, unintentional reflection occurs. To avoid this effect the size of the model has to be chosen large enough around the site of interest and suitable boundary conditions to attenuate or absorb the wave energy must be used.

The absorbing boundary condition (ABC) introduced by Mur calculates how an incident perpendicular wave would behave behind the boundary and subtracts the result. This simple method is only effective for perpendicular waves that is to say for arbitrary incident angles disturbing reflections still occur.

The Higdon radiation operator is the default ABC in *GprMax*. It involves the construction of a series of linear differential operators to annihilate outgoing numerical waves. It perfectly absorbs plane waves impinging on the boundary within a (in the operator) specified angle range $\pm\alpha_l$. The default operator in *GprMax* is of third order, which is sufficient for most simulations. If it is known that waves will impinge on the ABC in specific angles the operator can be optimized for those [Giannopoulos, 2002].

More effective and more general is the ABC introduced by Berenger, called *Perfectly Matched Layer* or PLM. It splits up Maxwell's curl equations 2.1.3 and 2.1.4 and introduces a magnetic conductivity σ^* in order to absorb waves effectively [Aulbert, 2000].

2.2 Some notes on FD-TD modelling

The model's extension in (x,y,z) should be several wavelengths larger than the region of interest. This prevents unintended reflection from the boundaries in addition to the ABC. The same applies for source and receiver positioning.

The spatial discretisation step Δ depends on the applied frequency of the source and the permittivity of the medium. A rule of thumb is to choose Δ at least ten times smaller than the shortest wavelength (wavelength in the medium with the highest

permittivity), in order to avoid numerical dispersion. Due to the fact that spherical, ellipsoidal and rough surfaces are approximated through Yee cells, Δ has to be small enough to render them properly.
The time step Δt mentioned at the end of section 2.1 is calculated automatically in *GprMax* from the *CLF* condition [Giannopoulos, 2002],

$$\Delta t \leq \frac{1}{c\sqrt{\frac{1}{(\Delta x)^2} + \frac{1}{(\Delta y)^2} + \frac{1}{(\Delta z)^2}}}. \tag{2.2.1}$$

2.3 Present model generators

The possibilities provided by commercially available GPR model generators will be presented using *GprMax* and *REFLEXW*.
The electromagnetic simulator for ground probing radar *GprMax* was written by A. Giannopoulos at the University of York and is freely available at `www.gprmax.org`.
The software enables the user to create 2-D and 3-D models. It is a text based application. The necessary input information for the GPR model contains an ASCII input file, while the output data is stored in binary or ASCII format. The program does not offer any visualization tools, thus an external program such as *MATLAB*, has to be used in order to display the models and results.
It is possible to create a variety of geometric shapes, e.g. boxes, cylinders, triangles and circular segments. Hence interfaces between different media are always smooth. An example for a subsurface model created with *GprMax* and plotted with *MATLAB* is shown in Figure 2.1.

REFLEXW was written by K.J. Sandmeier at the University of Karlsruhe as a processing software for GPR and seismic wave propagation. Field data as well as synthetic data can be processed in two and three dimensions. A variety of filters, gain, static corrections, spectral analysis and migration can be applied to the data. The software package also includes a modelling module for 2-D and 3-D models. The

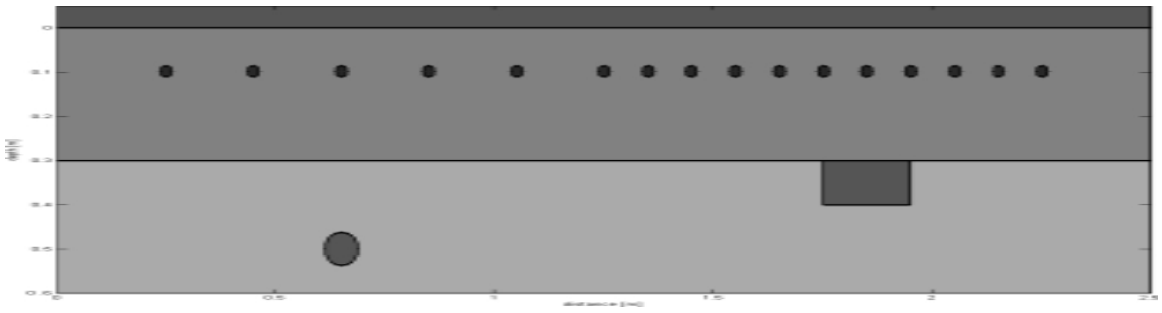

Figure 2.1: *Subsurface model created by GprMax2D. The model contains four different materials: free_space, sand, concrete and perfect electrical conductor (PEC). It is constructed from* box *and* cylinder *commands.*

structure of the model and its parameters can be edited interactively and instantly viewed on the screen. The model parameters are stored in binary format and the output data can be stored in binary or in ASCII format. Output data can be exported to the *REFLEXW* format and directly processed by the 2-D/3-D-data-interpretation modules.

The possible geometries for the model are similar to those provided by *GprMax*.

The disadvantage of all these model generators is that building complex models is very time consuming. Naturally inhomogeneous media can only be represented by effective dielectric properties. Placing small particles into a host medium will take time and never be statistically distributed.

Chapter 3

Statistical Modelling of Subsurface Media

3.1 Characteristics of discrete scatterers and rough surfaces

Subsurface media is in general a conglomeration of different sized particles with a variety of physical parameters and dielectric properties such as density and electrical permittivity. The random distribution of particles leads to rough interfaces between different media. If the wavelength of the electromagnetic waves passing through the subsurface is comparable in size to the roughness and heterogeneity of the media, propagation of the wave is effected. Scattering occurs at the interface which makes it difficult to interpret reflected signals recorded at a receiver. Examples of intrusions in the ground that cause scattering are water pipes, brine inclusions in snow and ice or fractal interfaces due to thawing and re-freezing.

Because of the great variety of geometric configurations it is mathematically difficult to describe these media. It is not sufficient to handle the physical and dielectric properties such as size or permittivity alone. Additional information about the statistical

spatial distribution and orientation of the inhomogeneities is required.

The statistical characteristics of a random rough surface are generally described by the standard deviation of surface height and the surface correlation length.

An arbitrary one-dimensional surface has height points $z(x)$ with a mean height $\bar{z}$.

$$\bar{z} = \frac{1}{N}\sum_{i=1}^{N} z_i \tag{3.1.1}$$

The discrete height distribution function is obtained by digitizing the profile into discrete values $z(x_i)$ at an appropriate spacing Δx. The standard deviation of surface height is then given by

$$h = \left[\frac{1}{N-1}\left(\sum_{i=1}^{N}(z_i)^2 - N(\bar{z})^2\right)\right]^{1/2} \tag{3.1.2}$$

where N is the number of samples.

The normalized autocorrelation function for a one-dimensional surface profile $z(x)$ is a measure of the similarity between the height z at point x and at a point x' afar from x. For the previously mentioned case the normalized autocorrelation function is given by

$$\rho(x') = \frac{\sum_{i=1}^{N+1-j} z_i z_{j+i-1}}{\sum_{i=1}^{N} z_i^2} \tag{3.1.3}$$

where $x' = (j-1)\Delta x$ and j is an integer ≥ 1 [Ulaby et al., 1982].

The correlation length l is then defined as the displacement x' for which $\rho(x')$ is equal to $1/e$. When two points are separated by a distant larger than l they can be considered statistically independent of each other [Ulaby et al., 1982].

A surface is considered smooth if its standard deviation of surface height satisfies the *Rayleigh criterion*,

$$h < \frac{\lambda}{8\cos\theta}. \tag{3.1.4}$$

Here λ is the wavelength in the medium and θ is the incident angle.

In the next section the characterization of a one-dimensional Gaussian random rough surface with a Gaussian correlation function will be described. Followed by a short

discussion about statistical spatial distribution of inhomogeneities in a host medium. The last section in this chapter will deal with the numerical realization and implementation of the statistic attributes into the FD-TD models.

3.2 Statistics of a random rough surface

A one-dimensional random rough surface is described by a height function $z = f(x)$, which is a random function of x with zero mean (Figure 3.1). The correlation function of the random process of surface height $f(x)$ is defined as

$$\langle f(x_1)f(x_2)\rangle = R_f(x_1, x_2) = h^2 C(x_1, x_2) \tag{3.2.1}$$

where h is the rms height and C is the correlation function of x_1 and x_2. Which is Gaussian in this example

$$C(x_1, x_2) = \exp\left(\frac{(x_1 - x_2)^2}{l^2}\right) \tag{3.2.2}$$

where l is the correlation length. As $|x_1 - x_2| >> l$, $C(x_1, x_2)$ tends to zero, and functions $f(x_1)$ and $f(x_2)$ become statistically independent.
The random height function is multiplied with the spectral density function in the frequency domain, in order to remove undesired frequencies. The spectral density function is defined as follows:

$$\Phi(k) = \frac{1}{2\pi}\int_{-\infty}^{\infty} dx R_f(x)\exp(ikx). \tag{3.2.3}$$

For the case of stationary Gaussian height distribution one yields

$$\Phi(k) = \frac{l}{2\sqrt{\pi}}\exp(-\frac{k^2 l^2}{4}). \tag{3.2.4}$$

An inverse Fourier transformation of the multiplication of height function and spectral density yields a complex vector. The real part is taken as the discrete function of the random rough surface. For closer studies I refer to [Tsang et al., 2000].

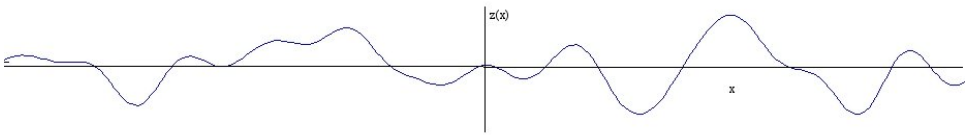

Figure 3.1: *One-dimensional Gaussian random rough surface.*

3.3 Statistical distribution of inhomogeneities in media

Specifying inhomogeneities in a host medium point by point becomes impossible for large numbers of scatterers. Therefore a statistical specification must be applied. For the inner geometry of the medium the following function can be defined

$$g(\vec{r}) = \begin{cases} 1 & \text{if } \vec{r} \text{ in the scatterer} \\ 0 & \text{if } \vec{r} \text{ elsewhere} \end{cases} , \tag{3.3.1}$$

differentiating between host medium and scatterer [Prager, 1961, Lim et al., 1994]. The fractional volume V_f is then defined by the volume average $\langle g \rangle$ of g itself:

$$V_f = \langle g \rangle = \frac{1}{V} \int_V g(\vec{r}) d\vec{r}. \tag{3.3.2}$$

The two-point average at position $\vec{r}$ and $\vec{r} + \vec{r}'$

$$S(\vec{r}') = \langle g(\vec{r}) g(\vec{r} + \vec{r}') \rangle \tag{3.3.3}$$

contains information about the shape of the inhomogeneities. It represents the probability that a line segment, having the length and direction of vector $\vec{r}'$ will, when thrown at random on an appropriate cross-section of the heterogenous material, land with both its ends in the intrusive medium [Prager, 1961] (Figure 3.2). The correlation function is then defined as

$$C(\vec{r}') = k \left(S(\vec{r}') - V_f^2 \right), \tag{3.3.4}$$

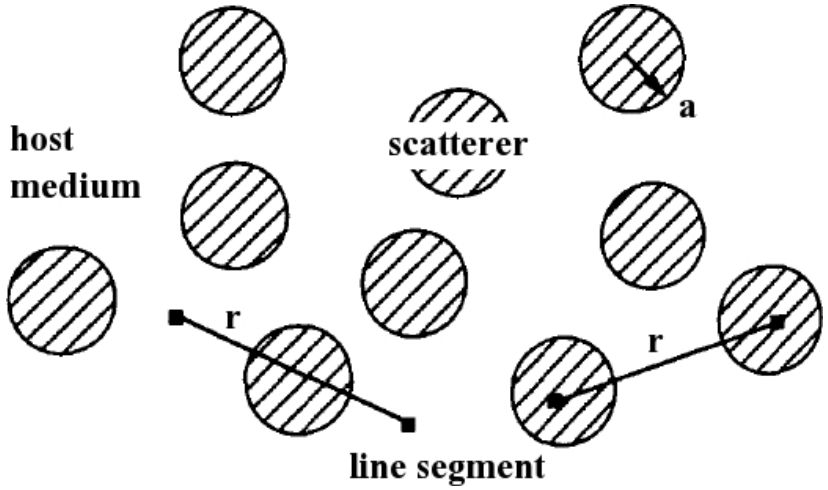

Figure 3.2: *Cross-section through a medium with spherical scatterers of radius a. The two line segments represent two different possible probability functions to describe the distribution of the scatterers.*

where k is a material property, e.g. the relative permittivity. The normalized correlation function, which is more common is defined as

$$R(\vec{r}') = \frac{C(\vec{r}')}{C(0)} = \frac{S(\vec{r}') - V_f^2}{V_f - V_f^2}. \tag{3.3.5}$$

Inhomogeneities are generally distributed uniformly within a specific volume. That means the probability to find a particle at one position in the volume is the same for the whole volume. The size and shape of the single scatterers can be described by a normal distribution with a mean radius and a corresponding standard deviation.

3.4 Implementation

Each geometrical object, defined in *modelGPR*, is made up of small rectangular elements, the Yee cells. After definition of total FD-TD grid size and discretisation in the space domain, a two- (or three-) dimensional cell array (the modelmatrix) of the size $N_x \times N_y (\times N_z)$ is generated, where each cell contains the string of the medium it simulates, initially *free_space* (see Figure 3.3 and page 61). The space coordinates

(x,y,z) are transformed into the matrix indices (i,j,k)

$$\begin{pmatrix} i \\ j \\ k \end{pmatrix} = \begin{pmatrix} x/\Delta x \\ y/\Delta y \\ z/\Delta z \end{pmatrix}. \tag{3.4.1}$$

air	air	air	air	air I,J
air i+1,j-1	air i+1,j	air i+1,j+1	air	air
soil i,j-1	soil i,j	soil i,j+1	soil	soil
soil i-1,j-1	soil i-1,j	soil i-1,j+1	soil	soil
soil 0,0	soil	soil	soil	soil

Figure 3.3: *Two-dimensional modelmatrix containing a medium-string in each cell.*

3.4.1 Random rough surface generation

Interfaces in the model have to be defined from top to bottom, because the actual layer overwrites the parameters of the previous one, when created. An interface between two media is defined by its depth z, rms height h, correlation length l_c, an eventual dip, the *seed* (see page 59) of the pseudo random number generator and the underlaying medium. With regard to the input parameters a discrete surface profile with $N = x_{total}/\Delta x$ samples is then generated ($N_x \times N_y$ samples in the 3-D case). Each surface height z_n at sampling point $n = 1, ..., N$ is transferred into a matrix index i. Afterwards all cells $c_{i,j}$ in the column j with an index smaller than i are allocated with the new medium string (see Figure 3.3 and page 61). If another interface

is assigned, it reallocates the cells it covers.
One-dimensional surface generation was briefly described in section 3.2 and an example shown in Figure 3.1. The two-dimensional random rough surface generation in *MATLAB* is solved in the following way.

Creation of two random matrices of size N with the command *randn*. The first matrix (R) provides the real part and the second matrix (I) the imaginary part of a new complex matrix

$$CM_{i,j} = R_{i,j} + iI_{i,j}. \tag{3.4.2}$$

The power spectral density (PSD) function is a Gaussian matrix

$$G = \sqrt{2\pi L} \cdot \sqrt{\frac{h^2 l_c \cdot \exp(-(k_x l_c \cdot 0.5)^2 - (k_y l_c \cdot 0.5)^2)}{2\sqrt{\pi}}}. \tag{3.4.3}$$

Where L is the real dimension of the surface in meter and k_x and k_y are the wave numbers in x and y direction.
The complex, random matrix CM is now multiplied with the PSD and the result is shifted (see page 62). In a 2-D Fourier transform the zero-frequencies are in the 'corners' of the matrix. Therefore the product of PSD and random matrix is quartered and each quarter is exchanged with its diagonal counterpart. The result is a low-pass filter (Figure 3.4).
An inverse Fourier transform is then applied to that matrix, filtering out the high frequencies in the random matrix. The real part of the Fourier transformed matrix serves as the discrete data of a random rough surface (Figures 3.4 and 3.5).

3.4.2 Generation of random sized and distributed ellipsoidal scatterers

Ellipsoidal intrusions within a specific layer are defined by the volume in which they occur, a mean semi-major (a) and semi-minor axis (b) plus standard deviations, the

seed and the fractional volume they take up.

The number of scatterers N_p with a mean volume (or area), which are needed to fill up the fractional volume within the defined volume is calculated. This number is then doubled to ensure N_p is large enough, even for a high standard deviation. Afterwards uniformly distributed random vectors of length N_p for x, y and z, as well as normally (Gaussian) distributed vectors with mean value and standard deviation for a and b are created. Therefore the internal *MATLAB* functions *rand* and *randn* are used (see page 63). The position and dimensions of each scatterer are then transferred into matrix dimensions. From the central point (I,J), in the two-dimensional case, the cells $J \pm N_a$ are addressed and $I \pm N_b(j)$ are allocated with the intrusion's medium string, where

$$N_a = \frac{a}{\Delta x} \tag{3.4.4}$$

and

$$N_b(j) = b \cdot \sqrt{1 - \frac{m_j^2}{a^2}}, \qquad m_j = \begin{cases} -N_a, ..., -1 & if \quad j < J \\ 0, ..., N_a & if \quad j \geq J \end{cases} . \tag{3.4.5}$$

This routine takes up more computer time than simply using the built in *cylinder* or *sphere* functions of *GprMax*, but ellipsoidal intrusions might be interesting for polarimetric radar sounding. Figures 3.6 and 3.7 show 2-D and 3-D examples of normal distributed ellipsoidal scatterers in a host medium.

Finally, after the geometry of the model is defined and a survey option chosen, the input file for *GprMax* is created. Each cell of the modelmatrix is translated into a *box* command *GprMax* can interpret containing the lower left and upper right corner of the Yee cell plus the medium string. The medium string refers to a medium defined in the default medium file *media.dat* and describes the dielectric properties of the cell.

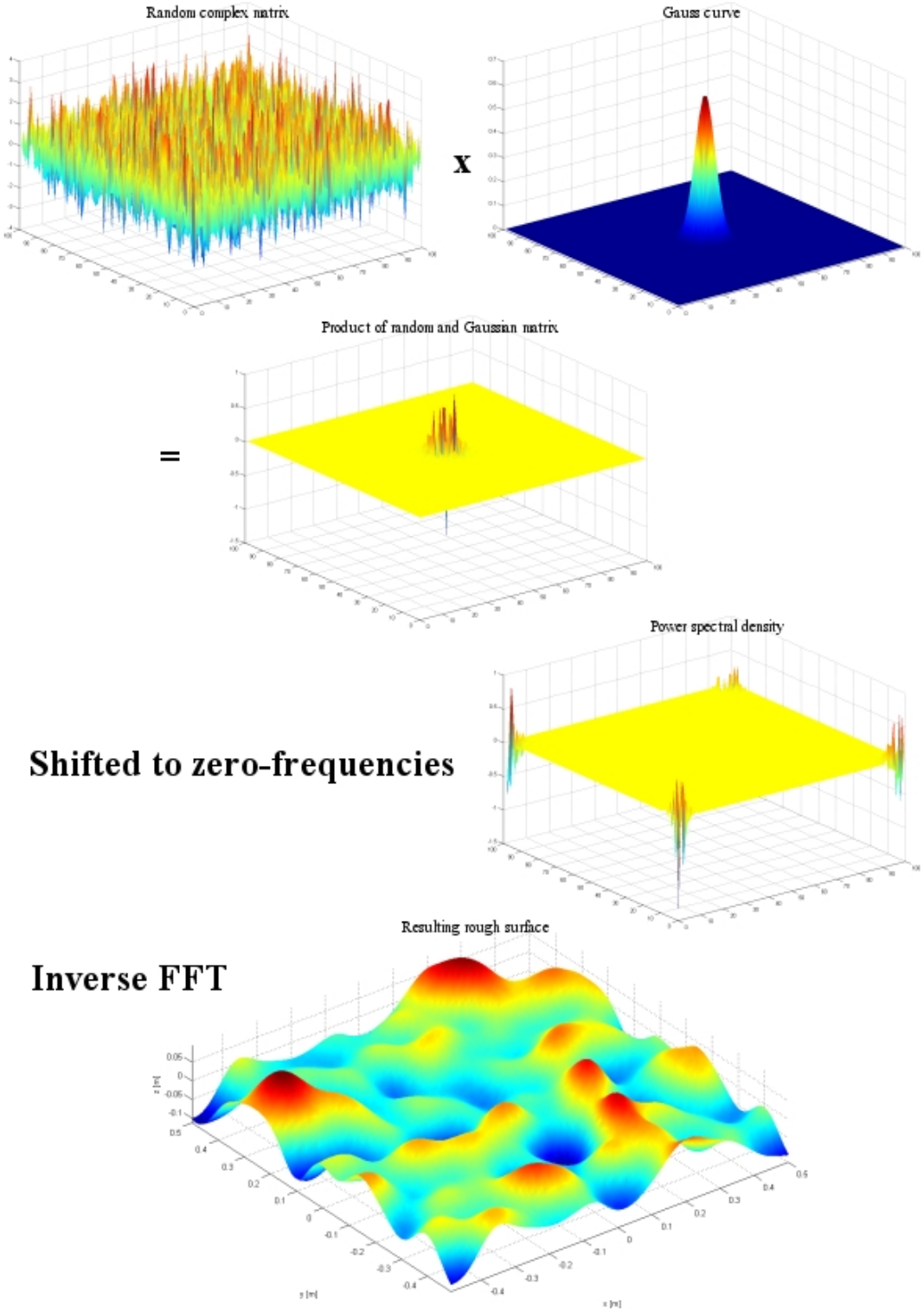

Figure 3.4: *2-D random rough surface generation: Multiplication of the PSD and the random, complex matrix in the Fourier domain and shifting the result to zero-frequencies. An inverse Fourier transformation yields the random, rough surface.*

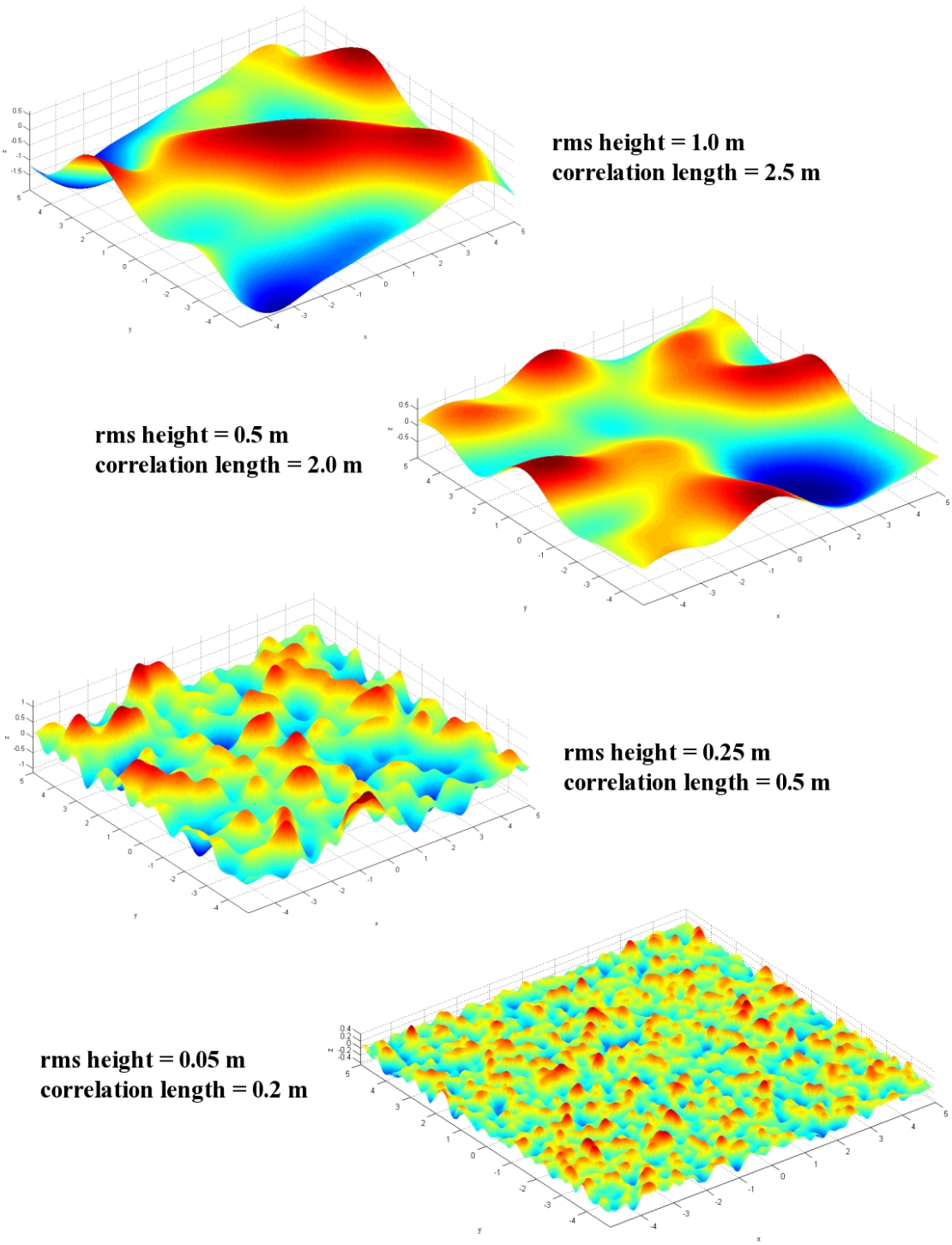

Figure 3.5: *Four example surfaces with different rms height and correlation length generated by the procedure described in section 3.4.1. All axes labels are in meter.*

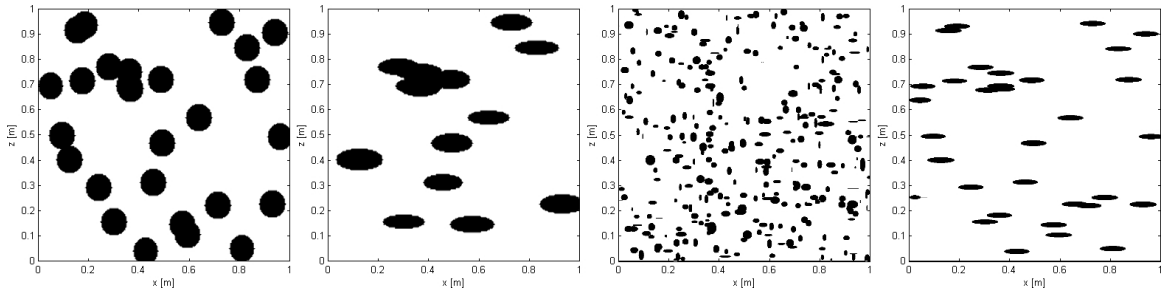

Figure 3.6: *2-D distribution examples of spherical and ellipsoidal scatterers (from left to right): Spherical scatterers with fractional volume V_f=20 % and mean radius r=5 cm; Ellipsoidal scatterers with V_f=10 %, a mean semi-major axis a=8 cm and a semi-minor axis b=3 cm; Mixture of spherical and ellipsoidal scatterers with V_f=10 % and r=1 cm; Flat, ellipsoidal scatterers with V_f=5 %, a=5 cm and b=1 cm.*

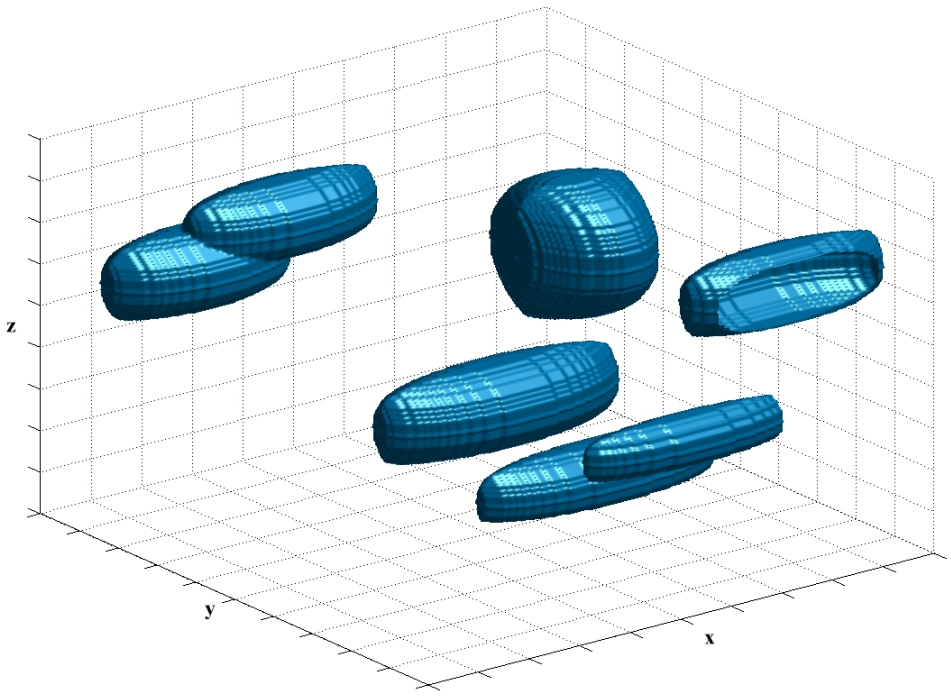

Figure 3.7: *Ellipsoidal scatterers with a=15 cm and b=5 cm. The standard deviation is 5 cm for both axes.*

Chapter 4

Radar Backscattering from a Svalbard Glacier

4.1 Introduction

Space-borne Synthetic Aperture Radar (SAR) has become an important tool in Earth observation. The fact that snow and ice are very radar friendly materials offers the possibility not only to map the surface but also get response from the shallow subsurface due to relatively good penetration of the electromagnetic waves.

The *EnviTools* project's [Guneriussen et al., 2002] intentions are to develop new methods for retrieval of cryospheric variables from Earth observation data in order to increase the usefulness of Earth observation data for environmental authorities and research. The overall aim is the development of transfer functions from SAR-facies to glacier facies that are effected by climate changes. The data can then be used in mass balance monitoring and modelling of future changes [Guneriussen et al., 2002]. The project combines SAR observation, GPR analysis and in-situ measurements of glaciers on Svalbard, Norway. The GPR will operate in the same frequency as the SAR (C-band: 5.3 GHz) and therefore see the same backscattering structure [Guneriussen et al., 2002]. Due to the fact that the SAR data contains no depth

information, but penetrates several meters into the ground, the backscattering coefficient is effected by shallow layering and structures. These scatterers, contributing to the SAR signal, will be unwrapped by the GPR. In order to calibrate the data, ice cores are taken along the GPR profile and snow depth is measured over the studied glaciers.

The ground-penetrating radar used was designed and constructed by Svein-Erik Hamran. It is a step-frequency, continuous wave design with a frequency range of 4.8 GHz to 5.8 GHz, center frequency of 5.3 GHz (C-band) [Hamran and Langley, 2004].

At these frequencies high resolution images of the subsurface are obtained, but also strong scattering occurs at the interfaces and in the layers making interpretation more difficult.

The aim of this chapter is to show how modelling can support analysis of the structures or layers that cause the scattering. First, different snow/ice interfaces with different rms heights and correlation lengths will be compared. Then small 2-D ice-models will be used to investigate the volume scattering.

4.2 Field campaign

I had the great opportunity to participate in the second *Envitools* field campaign on Svalbard at the end of April this year. The field site is Kongsvegen glacier in the northwest of Svalbard (small map in Figure 4.1).

Kongsvegen covers an area of 102 km^2, is about 25 km long and slopes gently from sea level to 800 m a.s.l. [Liestøl, 1988]. A center line profile of 9 stakes (Figure 4.1) with approximately 2.5 km spacing set-up by the Norwegian Polar Institute is used as the reference line for GPR profiles at different frequencies. Beside the GPR measurements, GPS elevation profiles were recorded and ice cores were taken at selected stakes (Figure 4.2).

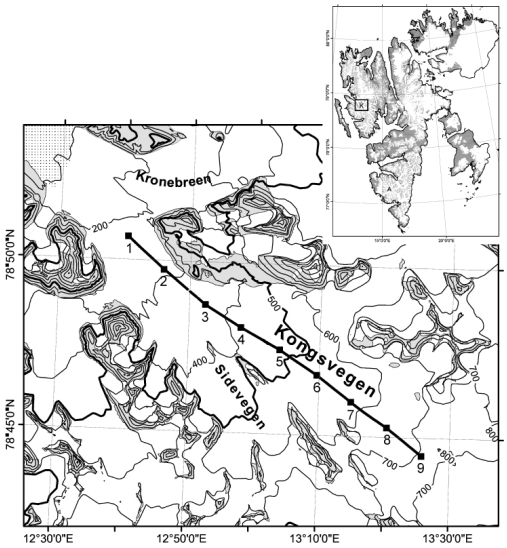

Figure 4.1: *Location of the field site. Kongsvegen glacier is separated into 9 stakes along which the profiles were recorded.*

Figure 4.2: *Impressions from the field work on Kongsvegen 2005: a) C-band GPR setup for a small scale 3-D grid survey. b) Data recovering from a GPS station. c) C-band and 800 MHz (orange sledge) GPR setup for profiles along the glacier. d) After drilling: cleaning the drill and examination of the core.*

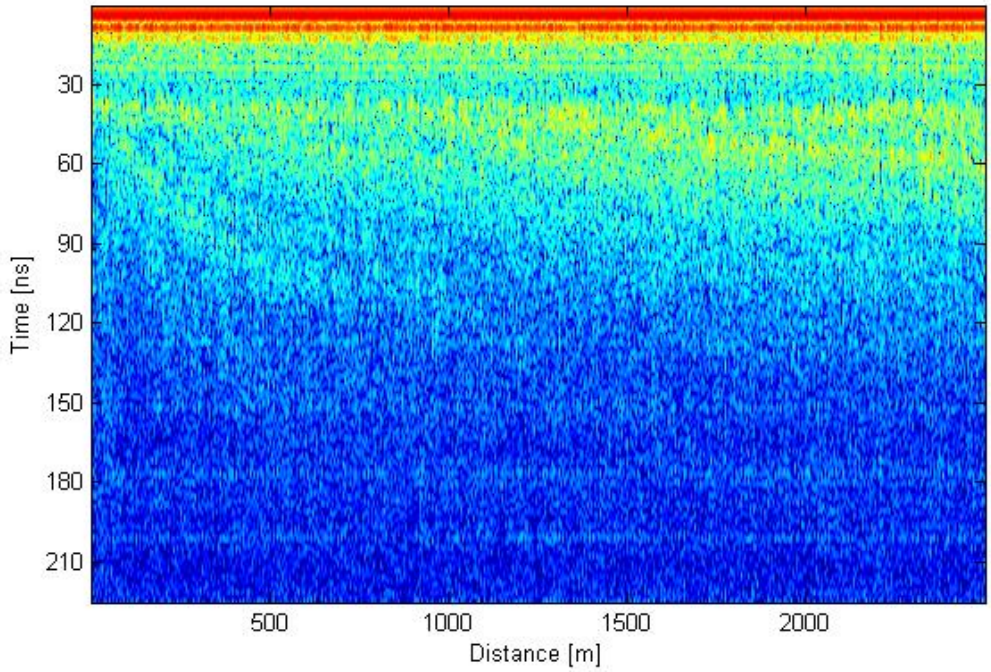

Figure 4.3: *GPR (C-band) profile from stake 7 to stake 8 on Kongsvegen. The colormap regards to the signal amplitude from 50 dB (blue) to 120 dB (red). Strong scattering occurs in the near-surface region.*

Figure 4.3 displays the signal amplitude in dB from a C-band GPR profile of the shallow subsurface from stakes 7 - 8 on Kongsvegen. Light colors correspond to strong backscattering. The first bright, continuous signal originates from last years summer layer, the overlying snow pack gives very little response [Langley and Hamran, 2005]. The increase in backscatter may be due to rough interfaces between snow and ice as well as transition zones between ice with different bubble contents. The air bubbles themselves could also contribute to the scattering.

4.3 Comparison of the response from different snow/ice interfaces

A simple two-dimensional grid of 1 m × 1 m with 2 mm spacing is the basis of the following models. An interface at 50 cm splits the area in two. The upper half has a relative permittivity of 1.7 and a conductivity of 0.01 mS/m and represents dry, airy snow. In the lower part the permittivity is 3.2 and the conductivity is 0.1 mS/m representing ice. The values are based on standard tables (e.g. in [Daniels, 2004]) and were chosen to ensure a significant permittivity contrast $\Delta\epsilon$. Thus $\Delta\epsilon$ between the two layers in all models is 0.5. The models are displayed in the left column in Figures 4.4 and 4.5. A radar scan with a center-frequency of 5.3 GHz at 10 cm depth in the snow layer is applied to each model. The scan involves 17 measurements from $x = 10$ cm to $x = 90$ cm with a 5 cm spacing. Its result is shown as a wiggle plot in the second column of Figures 4.4 and 4.5. The plots on the right hand side in Figures 4.4 and 4.5 show the amplitude of the signal from the center of the models (x=0.5 m / trace 9) in dB versus time.

The rms heights of the interfaces in models **1a-c** (Figure 4.4) are 0 cm, 2 cm and 5.6 cm respectively. The latter being a rms height comparable to the free air wavelength at 5.3 GHz. The correlation length in **1b** and **1c** is 10 cm.

As expected, the GPR receives a single strong signal from the flat surface in **1a**. The corresponding amplitude plot has a dynamic range of 60 dB and shows clearly the primary signal. The second amplitude at 5.8 ns results from non suppressed boundary reflections and is only visible due to the logarithmic scale.

Small variations in the surface height, like in model **1b** lead to reflections from the 'slopes' and result in a more complex signal response. This effect is even stronger in the very rough surface model **1c**, concluding that a standard deviation of the surface height of the size of the propagating wavelength leads to stronger disturbances in the signal.

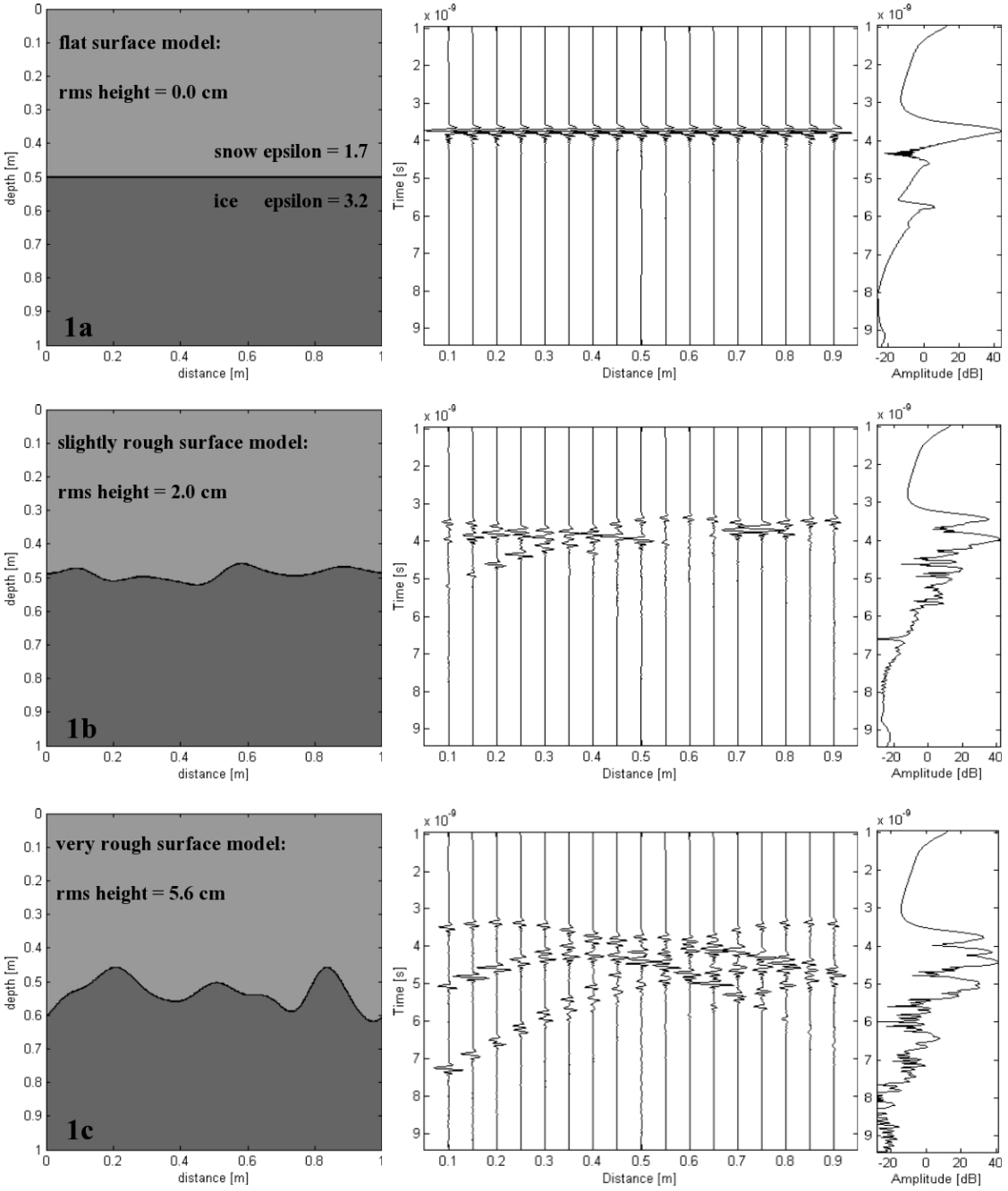

Figure 4.4: *Comparison of snow/ice interfaces with constant correlation length l=10 cm, but different rms surface heights. The models are shown in the left column. The corresponding wiggle plot of the signal from a 5.3 GHz GPR scan is displayed in the center column and the right column contains the amplitude in dB vs. time of the trace at 0.5 m from the wiggle window.*

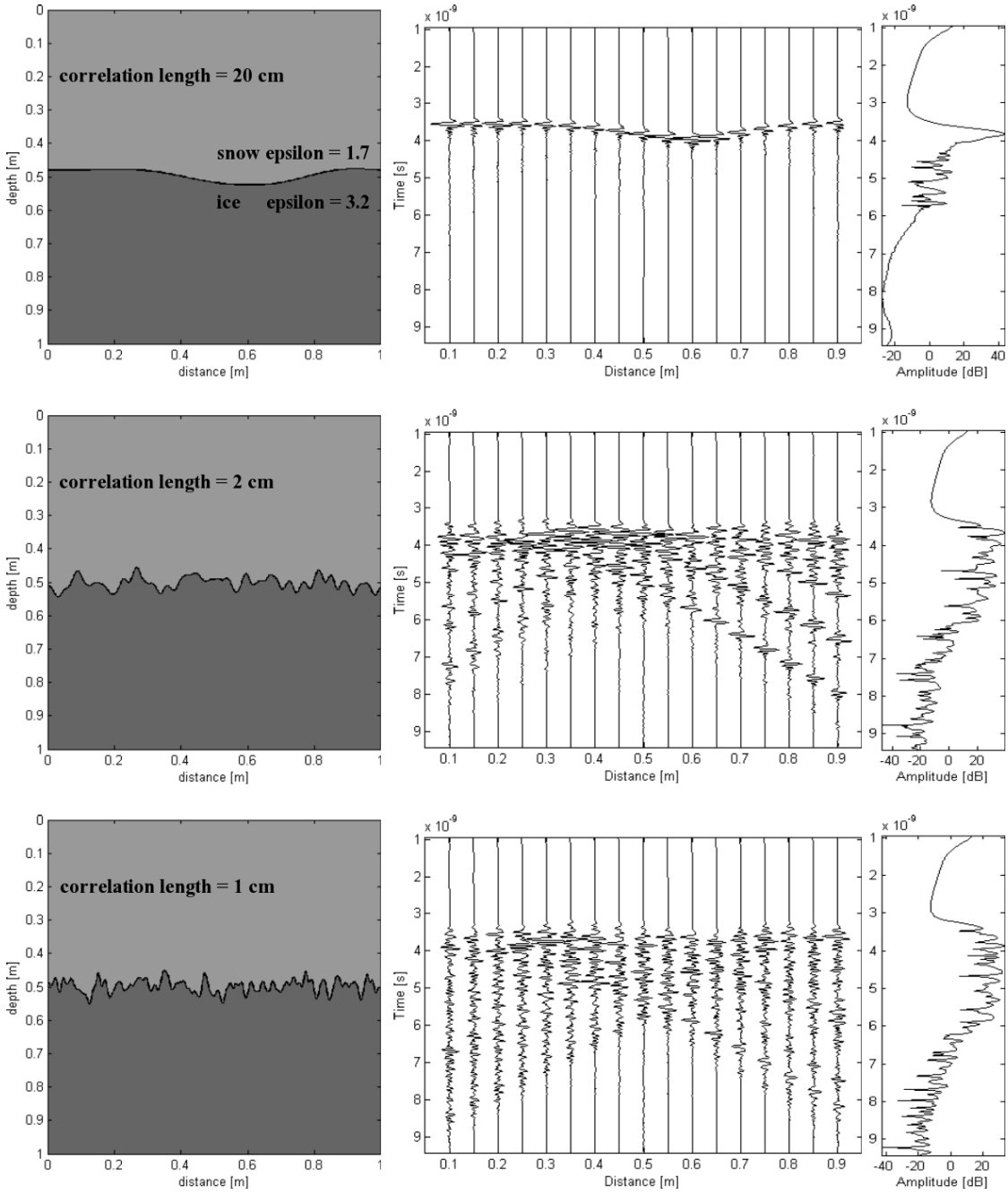

Figure 4.5: *Comparison of snow/ice interfaces with constant rms height h=2 cm, but different correlation lengths. The models are shown in the left column. The corresponding wiggle plot of the signal from a 5.3 GHz GPR scan is displayed in the center column and the right column contains the amplitude in dB vs. time of the trace at 0.5 m from the wiggle window.*

Changing the correlation length to smaller values makes the interface rougher. The rms height in the models **2a-c** shown in Figure 4.5 is now fixed at 2 cm and only the correlation length varies.

The interface is easy to identify in the wiggle plots of models **1b** (l_c =10 cm) and **2a** (l_c =20 cm). The primary reflection in the amplitude plots is two to three orders of magnitude larger than later 'slope-reflections'.

This behavior changes drastically as soon as the correlation length of the interface drops below the wavelength. In the models **2b,c** the correlation length is 2 cm and 1 cm respectively forming steep slopes on the surface. With l_c ten times smaller than in the previous models and less than half the wavelength, strong scattering occurs in the signal. The primary reflection is no longer dominating in the amplitude plot. Instead the signal amplitude is about 15 dB smaller, quite constant over several ns and decays relative slowly.

Considering these surface models, one feature that leads to the scattering observed in the GPR signal from Kongsvegen glacier could be snow/ice- and ice/ice-interfaces with correlation length smaller than the applied wavelength. Having a rms height comparable to the wavelength at the interface would increase scattering, too. In order to adjust the surface models to real snow/ice interfaces, their actual properties have to be known. But both, correlation length and rms height are difficult to obtain from a hidden layer.

In the next section potential volume scattering from air bubbles in the ice is investigated.

4.4 Backscattering from bubbled ice

Drilling at different spots on the glacier provides a glance at the geometry of the ice. Figure 4.6 shows a horizontal cross-section through an ice core at a depth of 33 cm (from the top of the first ice layer). The observable air bubbles, with diam-

eters from sub-millimeter to several millimeters, may contribute to the scattering. Based on visual interpretation I estimate the bubble content to be between 10-20 %. Unfortunately, no closer research on the cores has been done.

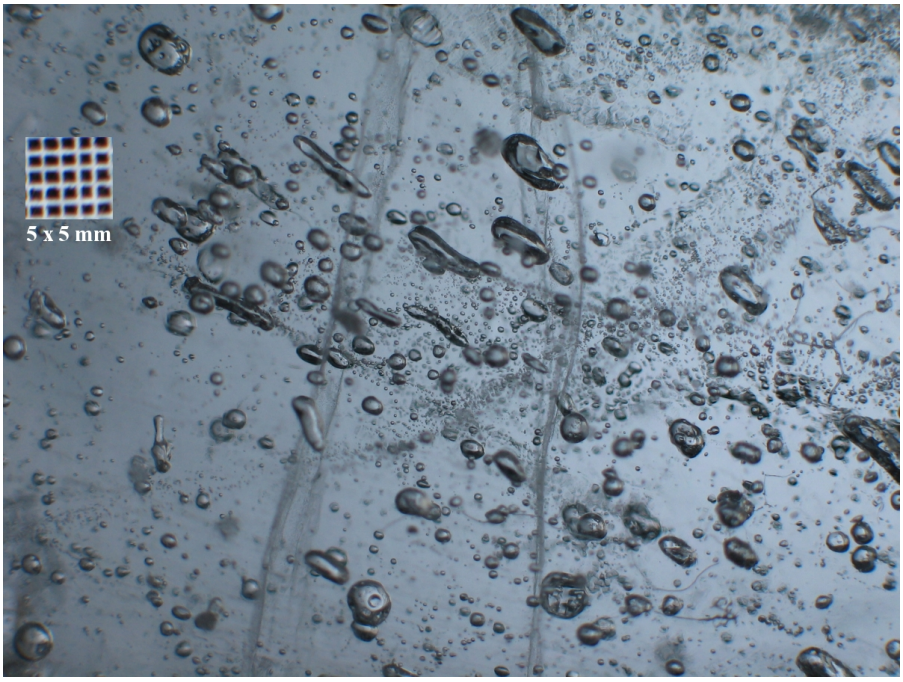

Figure 4.6: *Horizontal cross-section through an ice core at stake 3, Kongsvegen glacier from a depth of 33 cm in the first ice layer. The 5 x 5 mm grid on the left hand side shows the scale.*

In order to see if the air bubbles in the ice cause scattering of the propagating wave, models with different numbers of air bubbles n with mean bubble radius $\overline{r}$ will be investigated. The host medium is the ice medium used in the models in section 4.3. The model size is 0.5 m times 1.0 m with 2 mm cell spacing. Figure 4.7 shows all six models with their respective amplitude plots. The signal amplitudes are averaged over seven measurements from x=0.1 m to x= 0.4 m with 5 cm spacing and a total simulation time of 12 ns. The high amplitude events close to 10 ns in models **B**, **E** and especially **C**, **F** result from reflections at the bottom boundary. They are not visible in models **A** and **D** because a large bubble radius or a high number of scatterers leads to sufficiently strong attenuation of the wave.

The models **A** - **C** on the left hand side of Figure 4.7 have a constant number of scatterers n=50, but the mean radius varies from 2 cm to 0.5 cm. The signals have similar shapes and the dynamic range of the scattering signal is about 15 dB for all of them, but the signal amplitude decreases with smaller bubble radius. At 2 cm mean radius, amplitude peaks protrude to a maximum of 40 dB, whereas the maximum at 0.5 cm radius is at 28 dB. The average amplitude seems to drop by 4 - 5 dB with each bisection of the mean bubble radius.

In order to see how the number of scatterers effects the signal, models **C** - **F** have a constant $\overline{r}$ of 5 mm, but different numbers of scatterers are embedded in the host medium. The four models contain 200 (**D**), 100 (**E**), 50 (**C**) and 25 (**F**) single scatterers.

By examining the averaged signals, it can be seen that a decreasing scatterer number leads to a decrease of the average amplitude. The reduction in the mean amplitude after each bisection is slightly weaker than that for the radius bisection, i.e around 3 - 4 dB. In addition another effect appears. The dynamic range becomes narrower for higher numbers of scatterers. It is about 15 db for models **C** and **F** with small numbers of scatterers and decays to less than 10 dB for model **D** with 200 scatterers. One explanation could be, that in the case of many scatterers in the medium, the probability that a strong reflection from one particle is 'intercepted' and redirected by another one is more likely. On the contrary, scattering from a single scatterer in an elsewhere nearly homogeneous medium gains more weight in the whole scattering process and may result in a noticeable peak in the signal.

To conclude, amplitudes are weaker for smaller and/or fewer scatterers. Single high amplitude events are more likely for a small number of scatterers. The dynamic range of the signal (from within the intrusive medium) is smaller for many scatterers than when fewer scatterers are present.

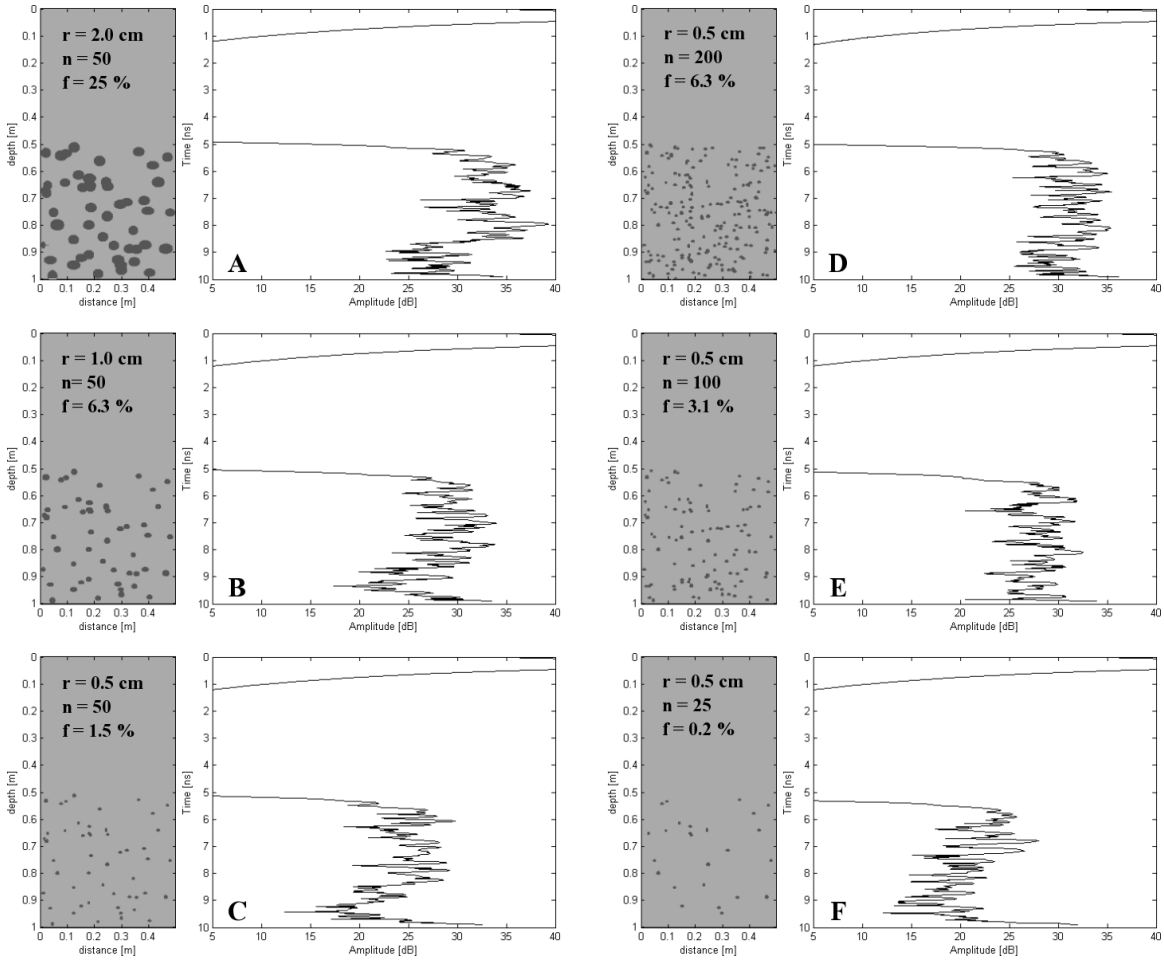

Figure 4.7: *Bubbled ice models: The left hand side contains the models with constant numbers of scatterers, but different mean bubble radius. On the right hand side the models with constant radius, but varying amount of scatterers are grouped. The amplitude plots are averaged over 7 measurements and focussed on the signal from the intrusions. The large amplitude around 1 ns results from the direct wave. Viewing the models from top to bottom shows a decaying average amplitude both with decreasing bubble radius, and decreasing number of scatterers.*

4.5 Future work

The models from section 4.3 and 4.4 give a first impression on what features could contribute to the backscattering observed on Kongsvegen (Figure 4.3). It is also possible to see how the signal changes under different circumstances: Surfaces with correlation lengths and rms heights smaller than the wavelength blur primary reflections; The mean radius and the number of scatterers effect the dynamic range and shape of the signal amplitude.

In order to reconstruct the real signal detailed information about surface properties, and bubble size and content from the different regions of the glacier have to be known. The model size must be large enough to cover all structures and layers effecting the GPR signal. The model generator will be used in the *Envitools* project by Kirsty Langley in order to fulfill the above requirements.

Chapter 5

Martian Shallow Subsurface Model

5.1 Introduction

The search for life on Mars has never been more intense than in the last years, largely driven by the increased ability to gather information from the surface and shallow subsurface of the planet. Several missions have been launched to investigate the Martian geology either from remote distances with orbiters, or directly by rovers dropped on the planet's surface. Current Mars missions are the 1996 Mars Global Surveyor, 2001 Mars Odyssee, Mars Express (ESA, Figure 5.1), and Spirit and Opportunity from the 2003 Mars Exploration Rover mission. Further missions are scheduled for the near future. For more details, pictures and videos see the reference webpages at the end of this chapter.

Ground-penetrating radar is a well suited and often applied tool for subsurface investigation in areas, which are difficult to access. In addition GPR performance is maximized when it is applied in very 'resistive' environments, as would be expected on a cold, dry planet [Pettinelli et al., 2003]. Ergo applying radar systems on Mars stands to reason.

The **WISDOM** experiment (**W**ater **I**ce and **S**ubsurface **D**eposit **O**bservation on **M**ars) a proposed component of the *Exomars* mission, is devoted to the exploration

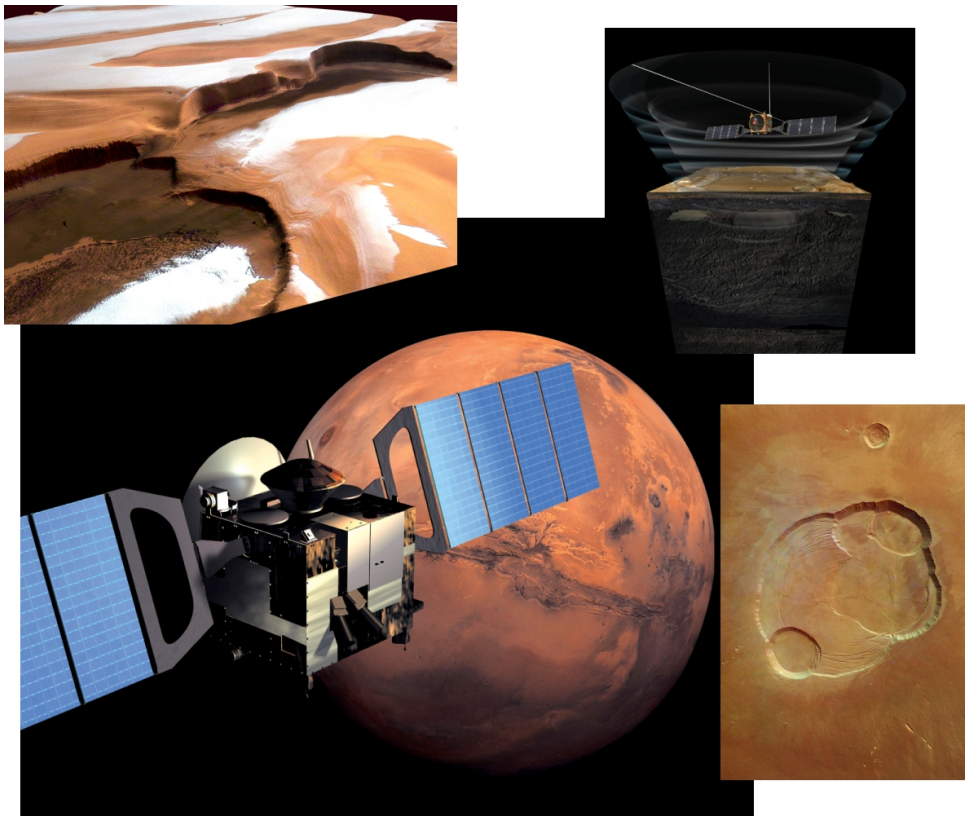

Figure 5.1: *Investigating Mars: The large picture shows ESA's Mars Express in the orbit of the planet. Small pictures clockwise: Ice and dust at Martian north pole recorded with the High Resolution Stereo Camera (HRSC); Ground-penetrating orbit radar (schematic); The Olympus Mons, the highest volcano in our solar system (HRSC). The pictures were taken from www.esa.int.*

of the subsurface and the search for water on Mars [Berthelier and Hamran, 2003]. It combines a set of three complementary instruments. Two electromagnetic tools, a Ground Penetrating Radar (GPR) and a Permittivity Probe (PP), to study the electrical properties of the soil, determine the structure and stratigraphy of the subsurface and search for water. And a third instrument (NITON) uses radioactive radon atoms in the atmosphere to yield information about the water content.

The GPR will operate in the very-high (VHF) and ultra-high frequency (UHF) range, in order to get information on larger structures to a depth of 50 m as well as to resolve details in the upper few meters of the Martian subsurface. In the UHF range the GPR should operate at a center-frequency of 2 GHz and will be mounted on the bottom

of the rover, approximately 25 cm above the ground. Its major issue is to access the structure, layering and electromagnetic properties of the shallow subsurface (comparable to the drilling range of the Permittivity Probe), with high resolution (few cm). Modelling of a GPR scan with a center-frequency of 2 GHz over a Martian-like subsurface could support system evaluation and give an idea of achievable penetration depth and potential results.

5.2 Model properties

The Martian two-dimensional model has a size of 10 m × 4 m and a discretisation in space of 5 mm, in order to get the typical value of 10 cells per wavelength in the most conductive medium. It consists of a flat soil layer over a dipping, slightly rough rock half-space. The soil layer will be riddled with rock intrusions of different size.
The Martian soil ranges from drift (sand) to cloddy with an average permittivity of 2.8, estimated from the average reflectivity of 6.4 % [Christensen and Moore, 1992] and measurements accomplished by the Viking Landers. Leuschen et al. (2003) observed that a soil sample can be decomposed into dry solid soil, iron oxide, air and water. Where water can exist as pure liquid water, salt water or ice.
Martian solid rock shows a high dielectric constant around 8 due to its low porosity [Leuschen et al., 2003]. Rocky particles from gravel size to large boulders can also be found in and on the upper soil layers. From surface observations, Leuschen et al. (2003) estimated their size to vary from 1 cm to 7 m.
The medium in the model will consist of two components, host medium and intrusions. Both will have an effective medium depending on their porosity and water saturation. The imaginary part of the permittivity is not taken into account. The thickness of the soil layer will vary from one meter on the left margin to 3.5 meters on the right margin.
Due to the fact that the dielectric properties of the Martian subsurface are only ap-

proximations and are not validated by samples covering representative, miscellaneous sites, the model will yield no variation in permittivity and only deal with the previously mentioned values for soil and rock/debris. Instead, the focus will be on how variation in size and distribution of the intrusions effects radar wave propagation. The conductivity of Martian soil might be quite significant because of the high iron concentration. Both media, soil and rock, will have a conductivity of 0.01 Sm^{-1} corresponding to an expected material loss of 20 dBm^{-1} [Berthelier and Hamran, 2003]. The same attenuation was evaluated by Pettinelli et al. (2003) for Martian icy soil.

5.3 Basic Martian model without intrusions

The model consists of three materials. The first layer, where the sources and receivers are situated, is free space. Next is a soil layer with a flat surface. The relative permittivity of the soil is 2.8 and the conductivity 0.01 Sm^{-1}. Below this lies a strongly dipping (14^o) rock half-space with a correlation length of 80 cm and a rms height of 15 cm. Permittivity and conductivity are 8.0 and 0.01 Sm^{-1}, respectively. The basic two-dimensional model is shown in Figure 5.2.

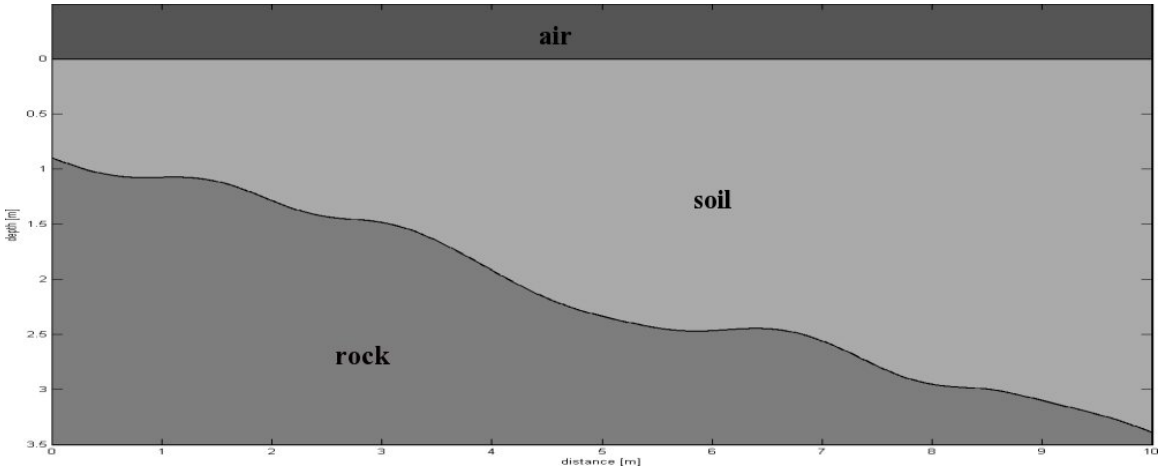

Figure 5.2: *Basic 2-D model of the Martian subsurface. Soil layer over a dipping bedrock.*

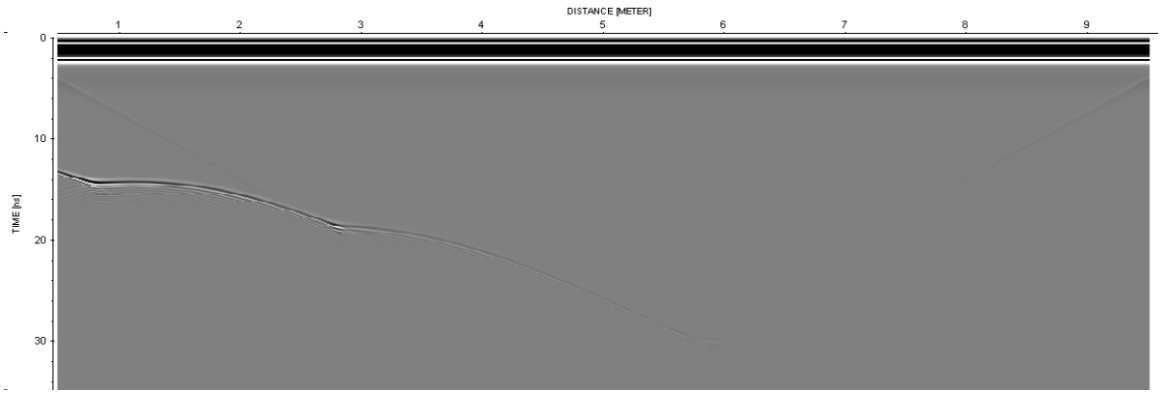

Figure 5.3: *Radar scan of the basic model with a sampling interval of 2 cm. High losses anticipate the investigation of structures below a TWT of 28 ns.*

The model is scanned with a center-frequency of 2.0 GHz and a sampling interval of 2.5 cm starting from 0.5 m. Each source is separated from its receiver by 1 cm. The total simulation time is 50 ns. Figure 5.3 shows the resulting radargram imported and displayed in *REFLEXW*. The data is unprocessed, only the plot scale is increased. The reflection from the dipping soil/rock interface can be followed until a two way travel-time (TWT) of 30 ns corresponding to a depth of 2.55 m. Deeper structures are hidden due to high losses in the soil layer. The diagonal incoming signals from the upper left and right margins are artefacts from the model boundaries.

5.4 Models with rock intrusions in the soil layer

The geometry is the same as for the basic model, but the soil layer is now riddled with rock intrusions. Figure 5.4 shows the model with rock particles with a mean radius of 4 cm and a fractional volume of 5 % in the soil layer. The same radar scan as in section 5.3 is applied to this model.
Now the signal (Figure 5.5) makes it difficult to identify the dipping rock interface. Single scatterers in the upper part of the soil generate clear diffraction hyperbolas and can be distinguished. Below 10 ns they become difficult to identify. The intense volume scattering prevents deep propagation and blurs the subsurface structure. In

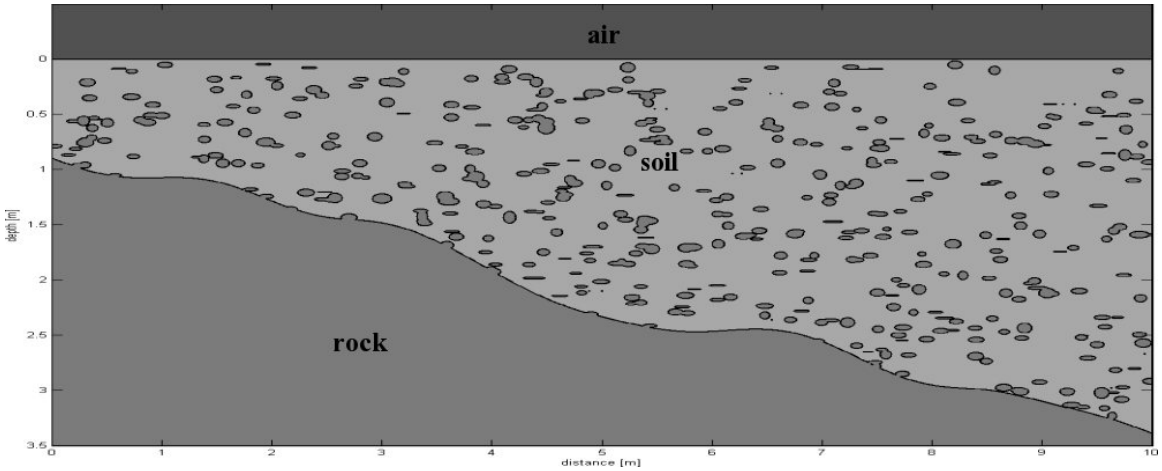

Figure 5.4: *Basic subsurface model plus a fractional volume of 5 % debris in the soil layer. The debris has the same permittivity as the underlaying rock and a mean radius of 4 cm.*

reality, erosion will probably lead to a smoother transition between debris and soil, and not such a strong permittivity contrast will be present. Hence, scattering would be less, but the energy of the incident wave at the soil/rock interface would still be strongly reduced.

Less volume scattering should occur if the intrusions are larger than the wavelength

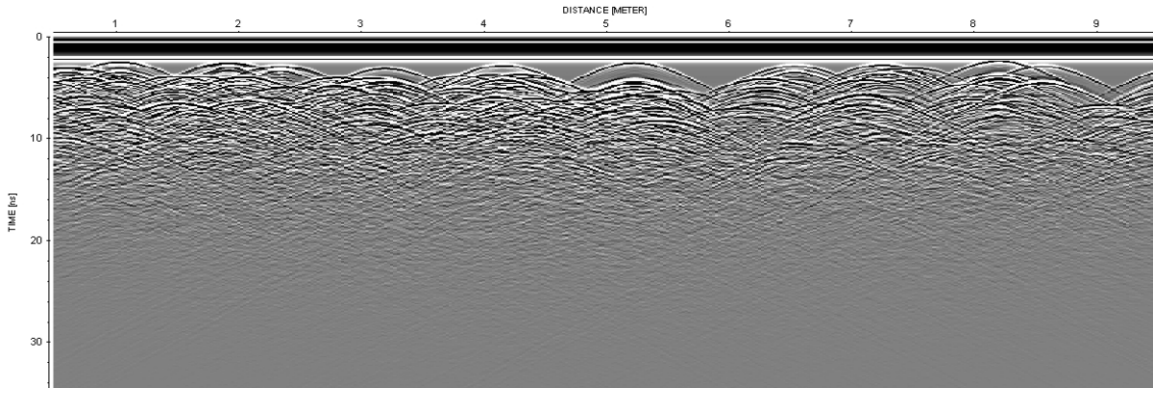

Figure 5.5: *Radar scan of the first intrusion model (Figure 5.4). Strong volume scattering blurs the dipping rock interface.*

and therefore material losses should be reduced, too. The second intrusion model (Figure 5.6) has fewer, but larger rock particles in the soil layer. Their diameters vary between 50 cm to 90 cm, which is six to eleven times the wavelength in the soil.

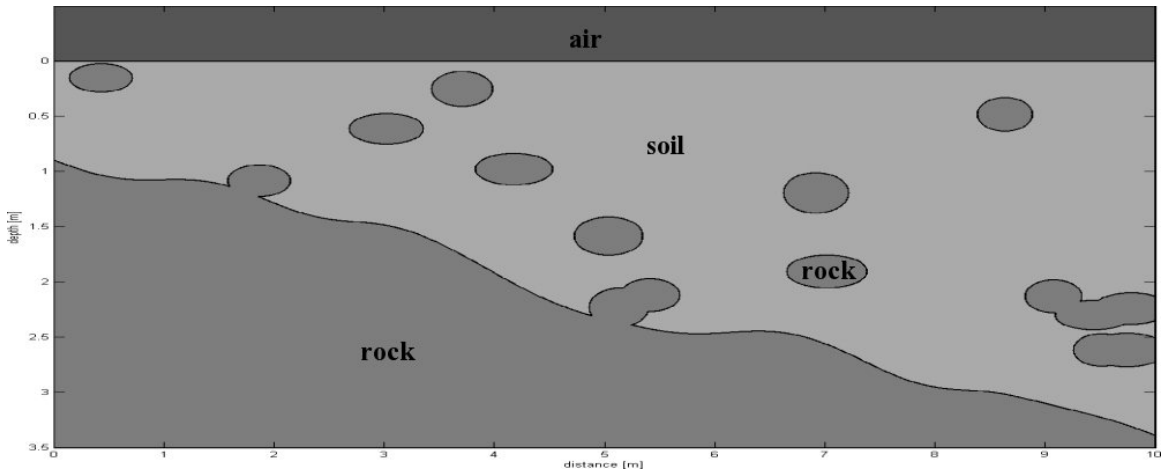

Figure 5.6: *Model with larger rock intrusions in the soil layer. Diameters vary between 50 cm to 90 cm and cover around 5 % of the total soil volume.*

The signal (Figure 5.7) from the model allows differentiation between almost all single scatterers, but identification of the soil/rock interface is still difficult. From the left margin to a distance of about 2.8 m reflections which originate from the soil/rock interface can be traced after migration (5.8). Afterwards multiple reflections from the overlaying intrusions make differentiations difficult.

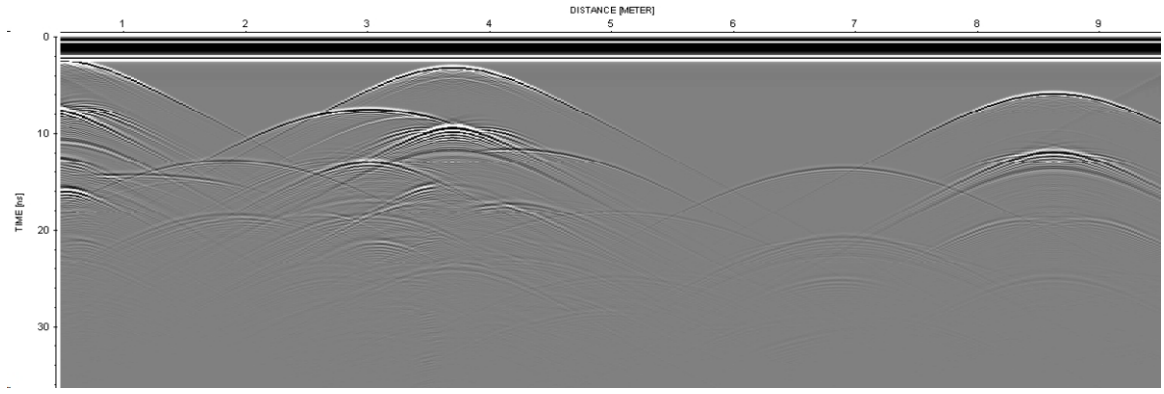

Figure 5.7: *Radar scan of the second intrusion model (Figure 5.6).*

The advantage of using spatially distributed scatterers in the model instead of having only a single effective medium offers the ability to compute more realistic signal response. Modelling without intrusions would have led to the conclusion that the identification of the soil/rock interface would be possible to a depth of about

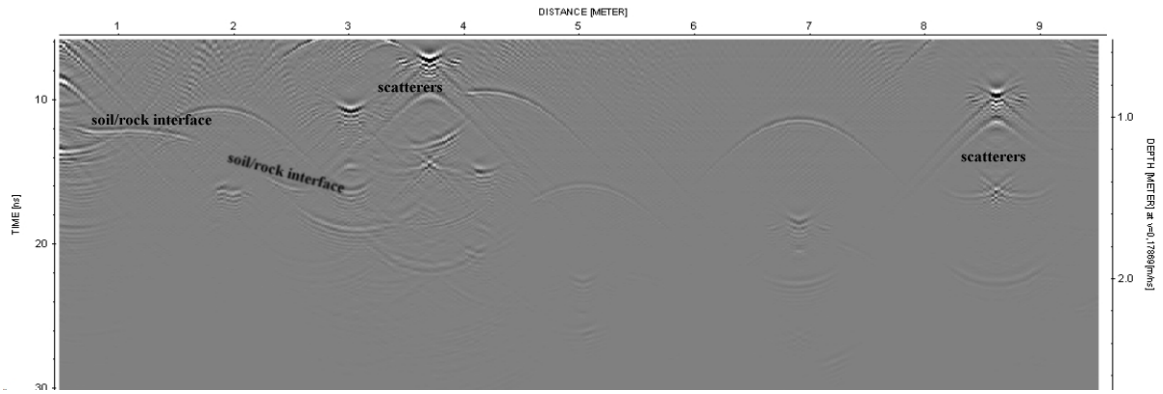

Figure 5.8: *The reflection from the soil/rock interface is visible in the shallow region on the left margin of the model after migration. Applied was a simple diffraction stack with an average velocity of 0,179 m/ns, which is the medium velocity of the host soil.*

2.5 m. Considering volume scattering from different scenarios shows that for large scatterers an identification is only possible to a depth of 1.3 m (Figure 5.8) and nearly impossible for numerous scatterers of size comparable to the wavelength.

5.5 Web pages on Mars missions

webpage	**comment**
http://nssdc.gsfc.nasa.gov/planetary/marsurv.html	NASA: 1996 Mars Global Surveyor mission
http://mars.jpl.nasa.gov/odyssey/	NASA/JPL: 2001 Mars Odyssee
http://marsrovers.jpl.nasa.gov/home/	NASA/JPL: Mars Exploration Rover Mission, Spirit and Opportunity rovers.
http://www.esa.int/SPECIALS/Mars_Express/	ESA: 2004 Mars Express
http://www.seds.org/~spider/mars/mars.html	Overview of current and future Mars missions.

Chapter 6

Conclusion

In this thesis I developed the statistical model builder *modelGPR*. It is capable of creating rough surfaces with given standard deviation of surface height and correlation length. The user can embed ellipsoidal inhomogeneities within a defined volume, where the important parameters are the mean semi-major- and semi-minor axis plus standard deviation, and the volume fraction occupied by the particles.
Currently the power spectral density function used to create random rough surfaces in my software is Gaussian. The distribution of inhomogeneities in the host medium is uniform and their size is governed by the mean value and standard deviation of a normal (Gaussian) distribution. It is possible to implement other distribution functions, but for naturally occurring surfaces, it is reasonable to assume a Gaussian distribution [Tsang et al., 2000]. The created model serves as an input file for the FD-TD software *GprMax* allowing the GPR response to the model to be calculate for various survey geometries.

The surface models in chapter 4 show how strongly the signal is effected by the surface roughness of an interface. Normal reflection occurs as long as the correlation length is larger than the wavelength, but strong scattering is provoked when wavelength and correlation length have the same dimensions (Figure 4.5). Knowledge of

the expected shape of a signal with respect to a given interface geometry can help to reveal single interfaces in real GPR data which are heavily blurred by surface scattering.

Investigation of composed media is generally done by weighting the dielectric properties of the single components with regard to their fractional volume and averaging them to receive an effective medium property [Olhoeft, 1989]. This procedure is a good approximation in media with intrusions much smaller than the applied wavelength. But, as soon as the inhomogeneities have a size comparable to the wavelength of the propagating wave, significant scattering and attenuation could occur, which would be suppressed by the use of an effective medium. The example of small intrusions in Martian soil (Chapter 5) shows that it is important to take the scattering effect into account when looking for layers beneath intrusion riddled media.

Furthermore is it possible to relate signal attributes, like maximum amplitude, dynamic range and attenuation to the quantity and shape of the inhomogeneities (Chapter 4). Although these relations are ambiguous, additional information can confine possible medium geometries and lead to a realistic interpretation.

The two example applications of *modelGPR* from chapters 4 and 5 have shown that using complex models simplifies the investigation of subsurfaces where intense scattering occurs. Scattering from either intrusions within a medium or the surface between two media can be studied independently in order to see how much each effect contributes to the entire signal response. The output of whole GPR profiles or single traces allows an overview as well as detailed signal studies.

The model builder will be used in the *Envitools* project [Guneriussen et al., 2002] in order to create larger and more complex models of the glacier's shallow subsurface, whose signals should be congruent with the ground response measured in the field. Such studies will enhance understanding of which structures or layers in the near-surface region have most effect on radar backscattering.

The model generator's application in an ESA proposed project is also planned for the near future. This will require further development and modification of *modelGPR*.

Acknowledgements

First of all I would like to thank my supervisor Svein-Erik Hamran for his guidance and help throughout the last year. He inspired me and raised my interest for GPR applications in Geosciences. Furthermore, he offered me the chance to participate in GPR related fieldwork and projects, which I really enjoyed.

Special thanks go to Kirsty Langley for the great teamwork. She was always helpful and put much effort in reviewing this thesis and refurbishing my English.

I am grateful for the reviews and comments from Christoph Marquardt, Dorothee Gaus and Mark Rieder, which were a great help.

Thanks go to Jon Ove Hagen, Jack Kohler, Rune Storvold, Kjell-Arild Hogda and Ola Brandt for the great time on Svalbard.

Last but not least I'd like to say thank you to Elisabeth Hilgers for her loving support and her steady belief in me.

Appendix A

modelGPR Manual

The model generator *modelGPR* enables the user to create an input file for the FD-TD software *GprMax* by Antonis Giannopoulos. Its purpose is to create subsurface GPR models with statistical properties, like interface roughness and spatially distributed inhomogeneities.
modelGPR does not cover the full capability of *GprMax* and is not a complete graphical user interface (GUI) for this text-based program. It rather extends it and simplifies complicated model building.
This manual deals only with the graphical user interface of *modelGPR*. An in-depth study of the original *GprMax* manual [Giannopoulos, 2002] is strictly recommended before working with *modelGPR*.

A.1 Getting started

Start *MATLAB* and open the folder *modelGPR*. Type *modelGPR* to start the program, a window opens up, which enables you to chose between the 2-D- or 3-D-version.

A.2 *modelGPR* 2-D version

This chapter describes the commands and functions of the 2-D version of *modelGPR*. Each section describes the commands of a single command window. Beginning with the essential commands, followed by the different survey types and the geometry options.

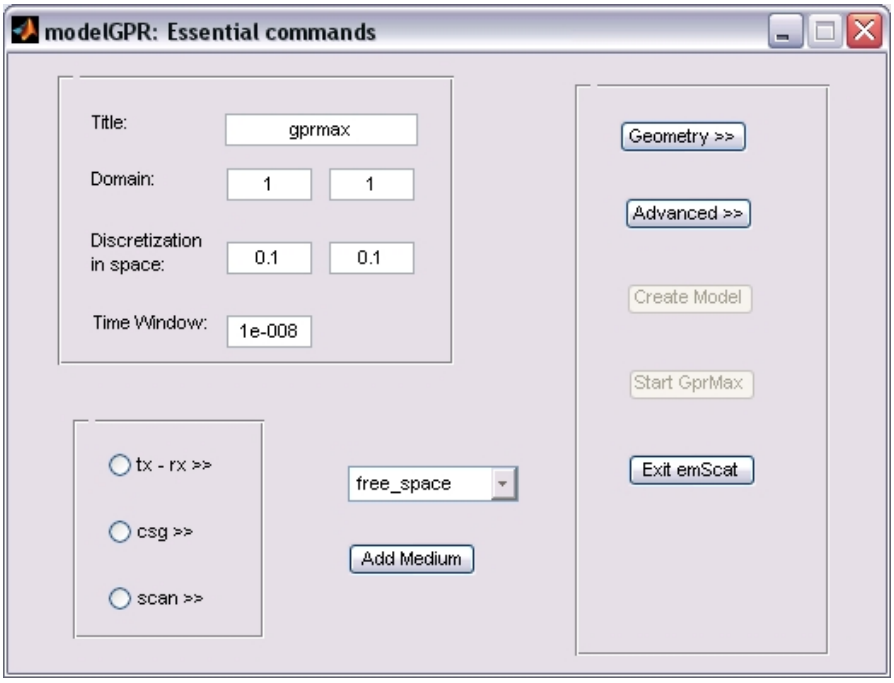

Figure A.1: *Main window for modelGPR 2-D, providing the essential commands which are necessary for a basic model.*

A.2.1 Essential commands

In the *Essential commands* window (Figure A.1) the upper left panel groups the four commands which are required by *GprMax2D* to run a basic model.

- `Title`: Enter the title of your model. The input file for *GprMax2D* will be the title plus the extension '.in'.

- `Domain`: Defines the size of the model in meter. The first value is the size in x-direction and the second the size in z-direction (or depth).

- `Discretisation in space`: Defines the size of the Yee cells in x- and z-direction for the finite-difference calculations in meter. This parameter is important for the accuracy of the calculation. The smaller the discretisation the more accurate the result, but the amount of required memory can increase enormously.

- `Time window`: Sets the total simulation time.

The radio buttons `tx - rx`, `csg` and `scan` define the survey type and open a new window.
On the right hand side, the push-buttons are grouped. `Geometry` and `Advanced options` open new windows. The `Create Model` button is enabled as soon as all necessary parameters, including essential commands, survey type and geometry, are set. After the creation of the model you can start the calculation in *GprMax* by clicking on `Start GprMax` (requires `gprmax2d.exe` at `C:\GprMax`).
The popup-menu lists all available media. Additional media can be defined with the `Add Medium` button.

A.2.2 Survey types

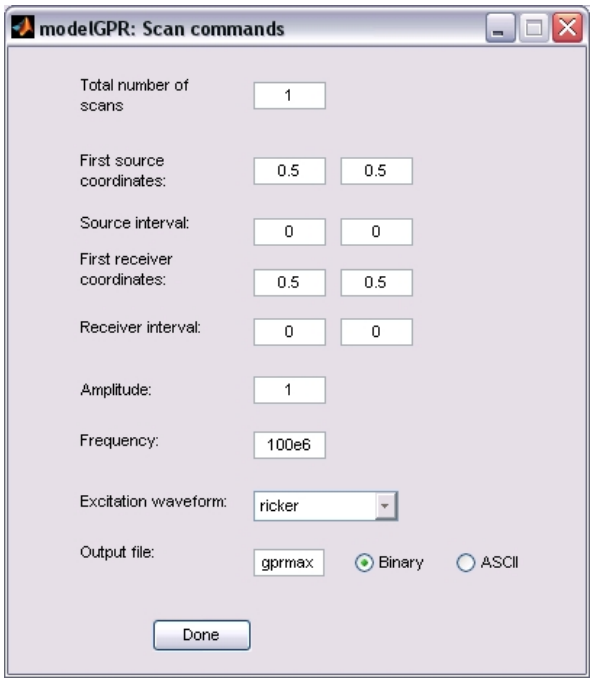

Figure A.2: *Scan window for modelGPR 2-D.*

There are three different survey types for *modelGPR*. A single source and receiver (tx - rx) configuration, a common source gather (csg) and a radar scan (scan) with several sources and receivers. Figure A.2 shows the input parameters for the scan option. Following commands are common to all three survey types.

- `Amplitude`: Sets the amplitude in ampere of the line source's current.
- `Frequency`: Sets the frequency in Hertz of the source excitation waveform.
- `Excitation waveform`: Defines the source excitation waveform.

- `Output file`: Insert the name of the output file without extension. The generated output will be stored in 'filename.out'. The radio buttons decide if the output file format is binary or ASCII.

In addition to these commands the geometry of the survey has to be defined. For the tx-rx option only the coordinates of the source and the receiver have to be set. For the common source gather, the location of the source and the first receiver must be defined, as well as the total number of receivers. The distance between the remaining receivers must also be set.
In the scan window (Figure A.2) the total number of scans and the interval between them, as well as the location of the first source-receiver couple must be set. The other scans are then placed according to the interval settings.

- `Total number of scans/receivers`: Defines the number of scans or the number of receivers in case of a common source gather (csg, scan).
- `(First) source coordinates`: Define the x- and z-coordinates of the source in meter (tx-rx, csg, scan).
- `(First) receiver coordinates`: Define the x- and z-coordinates of the receiver in meter (tx-rx, csg, scan).
- `Source interval`: Sets the spacing between the single sources in meter (scan).
- `Receiver interval`: Sets the spacing between the single receivers in meter (csg, scan).

A.2.3 Geometry

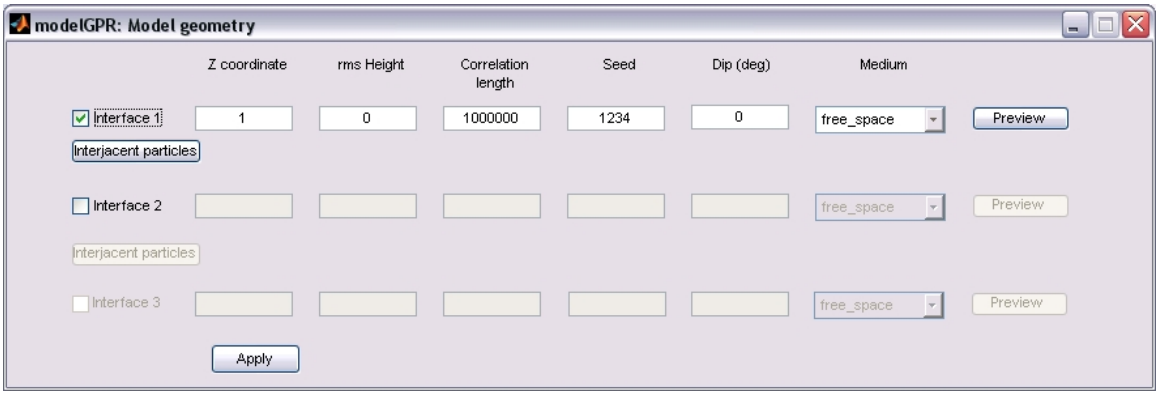

Figure A.3: *Interface geometry window for modelGPR 2-D.*

The `Geometry` button in the *Essential Commands* window opens up the *Model Geometry* window. Here the properties of rough interfaces and inhomogeneities can

be set.
The checkboxes enable the property edit boxes, in order to set the desired values for each interface.

- `z-coordinate`: Defines the depths of an interface. Note that the lower left corner in a *GprMax* model is the origin (0,0). So the shallowest layer has the highest 'depth' value. Due to the manner the layers are inserted in the model, 'Interface 1' has to be the highest z-coordinate, followed by 'Interface 2' and so on.

- `rms Height`: Standard deviation of surface height of the interface in meter.

- `Correlation length`: Correlation length of the interface in meter.

- `Seed`: Sets the value for the pseudo random number generator to ensure a repeatable result .

- `Dip`: Defines the dip of the interface in degrees. For a positive value the interface dips downwards from the left margin at the defined z-coordinate to the right margin. A negative value results in an upward going slope.

The popup-menu offers a choice of all previously defined media which are stored in the default file *media.dat*. After setting all parameters the defined surface can be viewed by pushing the `Preview` button.
In order to get a smooth interface set the `rms Height` to zero and the `Correlation length` to a very large number.

Intrusions in a layer can be defined in the *Intrusion Geometry* window in Figure A.4 after clicking the button `Interjacent particles`. The upper bound is automatically set to the z-coordinate of the overlaying interface. If no deeper interface is defined the lower bound is set to zero and the whole remaining area is considered as the area of interest. In case of a previously defined lower interface, the lower bound edit box contains its z-coordinate.

- `Fractional volume`: This value defines the amount of space, which the particles should take up of the whole volume. The whole volume is defined as the model's total x-extension times the upper minus the lower bound

$$V_{layer} = x_{total} \cdot (b_{upper} - b_{lower}) \,. \tag{A.2.1}$$

  If one or both of the interfaces have a dip the bounds and the fractional volume have to be chosen carefully.

- `Mean semi-major(-minor) axis`: The size of the particles is normally distributed around a mean value. Ellipsoidal particles have a semi-major and semi-minor axis. The values can be set here in meter.

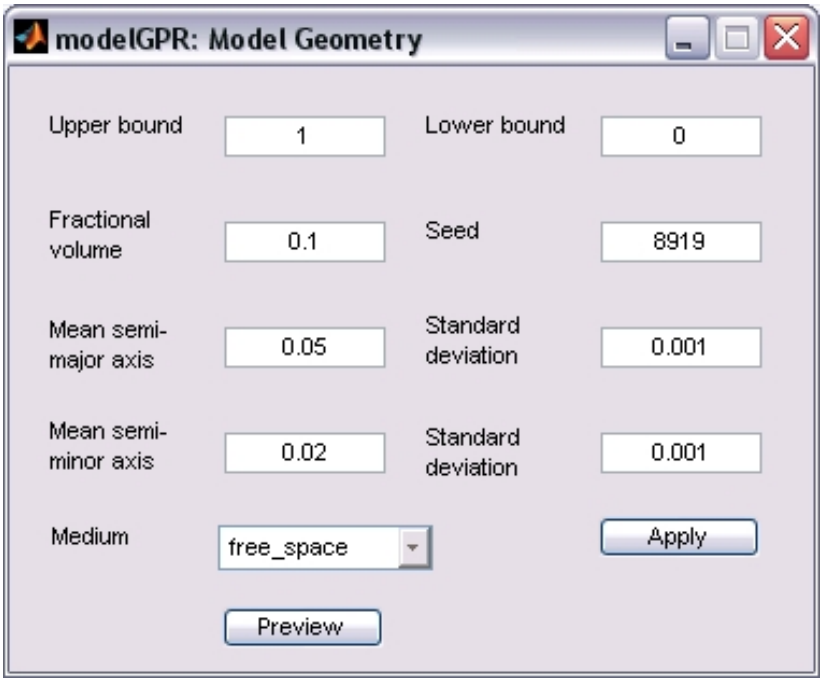

Figure A.4: *Intrusion geometry window for modelGPR 2-D.*

- `Standard deviation`: Sets the standard deviation of the mean value to its left.

The popup-menu gives the option to select the intrusive medium.

A.3 *modelGPR* 3-D version

The input parameters for the three-dimensional version of *modelGPR* are very similar to the 2-D programm. The main difference is, of course, the extension into the third dimension.
In the *Essential commands* window, model size and discretisation will be the same for the x- and y-direction, because the rough surface generation works only for square matrices.
In the survey windows all source and receiver coordinates and the eventual interval steps must now be defined in x, y and z. Beside that, the polarization of the source can be selected now.
The options in the *Geometry window* are the same as for the 2-D version.

Appendix B

MATLAB Functions

modelmatrix.m

```
function [modmat,N_cell] = modelmatrix(domain,dx_dy)
% Initialize the cell matrix of the model

Nx = domain(1)/dx_dy(1);
Ny = domain(2)/dx_dy(2);
N_cell = Nx*Ny; % number of cells

modmat = cell(Ny,Nx);

for i=1:Ny,
    for j=1:Nx,
        modmat{i,j}='free_space';
    end
end
```

roughS2D.m

```
function model = roughS2D(model,domain,dx_dy,interface,layer)
% This function creates a rough surfaced layer into the model.
% 'depth' is the given depth of the layer in meters in the model.


depth=layer.zcoord;
medium=layer.medium;

Nx=domain(1)/dx_dy(1);
```

```
Ny=domain(2)/dx_dy(2);

% Transfers the depth in meters into the (i,j) system of the matrix
baseline=round((domain(2)-depth)/dx_dy(2));

%creates a layer
for j=1:Nx,
    cval=baseline-round(interface(j)/dx_dy(2))+1;
    if cval>=0 & cval<=Ny,
        for i=cval:Ny,
            model{i,j}=medium;
        end
    end
end
```

grs2d.m

```
function [interface,x,y]=grs2d(N,rL,layer)
% grs2d creates a random rough surface in the x-y plane.

h=layer.rmsh;
lc=layer.lc;
seed=layer.seed;

randn('seed',seed);
x=randn(N);
y=randn(N);

CM=zeros(N);
for m=1:N
    for n=1:N
        CM(m,n)=complex(x(m,n),y(m,n));
    end
end


[x,y]=meshgrid(linspace(-rL/2,rL/2,N));
kx=2*pi*x./rL;
ky=2*pi*y./rL;
G=zeros(N);
G=sqrt(2*pi*rL)*sqrt(h^2*lc*exp(-(kx*lc*0.5).^2-(ky*lc*0.5).^2)/(2*sqrt(pi)));
```

```
b=CM.*G;
M=zeros(N);

for r=1:N/2
    for c=1:N/2
        M(r+N/2,c+N/2)=b(r,c);
        M(r,c)=b(r+N/2,c+N/2);
    end
end
for r=1:N/2
    for c=N/2+1:N
        M(r+N/2,c-N/2)=b(r,c);
        M(r,c)=b(r+N/2,c-N/2);
    end
end

FT=ifft2(M,N,N);
FT=FT.*N/rL;
interface=real(FT);

dx=rL/N;
x=[-N/2+1:1:N/2]*dx;
y=[-N/2+1:1:N/2]*dx;

figure; surf(x,y,interface); xlabel('x');ylabel('y');
axis('equal'); shading('interp');
```

particles.m

```
function part=particles(volume)

part=cell(zeros(1,5));

% x-coordinates %
Lx=volume.Lx;
xseed=volume.seed;

% z-coordinates %
UB=volume.ub; % upper bound of z
LB=volume.lb; % lower bound of z
zseed=xseed+55;
```

```
% semimajor-axis %
a_mean=volume.am;
a_std=volume.astd;
aseed=xseed+190;

% semiminor-axis %
b_mean=volume.bm;
b_std=volume.bstd;
bseed=xseed+123;

Vf=volume.Vf; % fractional volume
Vf=(Vf*(UB-LB)*Lx);
Np=2*round(Vf/(pi*a_mean*b_mean)); % number of scatterers

rand('seed',xseed);
x=Lx.*rand(1,Np); % uniformly distributed
rand('seed',zseed);
z=LB+(UB-LB).*rand(1,Np); % uniformly distributed
% normally distributed with mean a_mean and standard deviation a_std !!!
randn('seed',aseed);
a=a_mean+a_std.*randn(1,Np);
% normally distributed with mean b_mean and standard deviation b_std !!!
randn('seed',bseed);
b=b_mean+b_std.*randn(1,Np);

Vpart=0; i=1;

while Vpart <= Vf
    Vpart=Vpart+a(i)*b(i)*pi;
    i=i+1;
end

Np=i;

k=1;
for m=1:Np
    part{k}={[x(m),z(m),a(m),b(m)],volume.medium};
    k=k+1;
end
```

intrusion.m

```
function model=intrusion(model,domain,dx_dy,part)

dx=dx_dy(1);
Nx=domain(1)/dx;
Nz=domain(2)/dx;

J=round(part{1}(1)/dx);
I=Nz-round(part{1}(2)/dx);
a=round(part{1}(3)/dx);
if a==0
    return
end
b=round(part{1}(4)/dx);
m=a;

for j=J-a:1:J+a
    if j>0 && j<=Nx
        %spherical
        %for i=(I-round(sqrt(a^2-m^2))):1:(I+round(sqrt(a^2-m^2)))
        % ellipsoidal
        for i=(I-round(b*sqrt(1-m^2/a^2))):1:(I+round(b*sqrt(1-m^2/a^2)))
            if i>0 && i<=Nz
                model{i,j}=part{2};
            end
        end
        if j<J
            m=m-1;
        else
            m=m+1;
        end
    end
end
```

Appendix C

Contents of the CD-ROM

The attached CD-Rom contains the following folders:

Thesis

Contains this thesis in pdf-format plus all figures in jpg-format.

modelGPR

Contains the model builder *modelGPR* in the 2-D and 3-D version. Additional *MATLAB* functions for displaying the models and results are also present in the this folder.

GprMaxV1.5

The FD-TD software from A. Giannopoulos. The programm is also available at `www.gprmax.org`.

GlacierModels

This folder contains the input, output and geometry files for all glacier models discussed in chapter 4.

MartianModels

This folder contains the input, output and geometry files for the Martian models discussed in chapter 5.

Bibliography

[Aulbert, 2000] Aulbert, C. (2000). Effizient absorbierende Randbedingungen in numerischen Bodenradarsimulationen mittels Generalized Perfectly Matched Layers. Master's thesis, TU Braunschweig.

[Balanis, 1989] Balanis, C. A. (1989). *Advanced Engineering Electromagnetics*, chapter Electrical properties of matter, Wave equation and its solutions, pages 42–126. John Wiley & Sons.

[Berthelier and Hamran, 2003] Berthelier, J. J. and Hamran, S. E. (2003). WISDOM - Water Ice and Subsurface Deposit Observations on Mars. Proposal to ESA in response to the call for ideas for the PASTEUR payload.

[Christensen and Moore, 1992] Christensen, H. H. and Moore, H. J. (1992). *Mars*, chapter The Martian surface layer, pages 696–729. Univ. of Ariz. Press, Tucson.

[Daniels, 2004] Daniels, D. J., editor (2004). *Ground Penetration Radar, 2nd Edition*. The Institution of Electrical Engineers, London.

[Giannopoulos, 2002] Giannopoulos, A. (2002). *GprMax2D V 1.5 User's Manual*.

[Guneriussen et al., 2002] Guneriussen, T., Malnes, E., Hamran, S. E., Hagen, J. O., and Kohler, J. (2002). New spaceborne radar methods for glacier characterisation as tools for artic environment and resource monitoring. Project description.

[Hamran and Langley, 2004] Hamran, S. E. and Langley, K. A. (2004). A 5.3 GHz step-frequency GPR for glacier surface characterisation. In *Tenth International Conference on Ground Penetrating Radar*.

[Kozlov et al., 2001] Kozlov, A., Ligthart, L., and Logvin, A., editors (2001). *Mathematical and physical modelling of microwave scattering and polarimetic remote sensing*, chapter Physical and Mathematical Modelling, pages 43–65. Kluwer Academic Publishers.

[Langley and Hamran, 2005] Langley, K. A. and Hamran, S. E. (2005). Use of C-band ground penetrating radar to determine backscatter sources within glaciers. Submitted to IEEE Transactions on Geoscience and Remote Sensing.

[Leuschen et al., 2003] Leuschen, C., Clifford, S., and Gogineni, P. (2003). Simulation of a surface-penetrating radar for Mars exploration. *Journal of Geophysical Research*, 108(E4).

[Liestøl, 1988] Liestøl, O. (1988). The glaciers in the Kongsfjorden area, Spitsbergen. *Det Norske Geografiske Tidsskrifte*, 42:231–238.

[Lim et al., 1994] Lim, H. H., Veysoglu, M., Yueh, S. H., Shin, R. T., and Kong, J. A. (1994). Random medium model approach to scattering from a random collection of discrete scatterers. *Journal of Electromagnetic Waves and Applications*, 8(7):801–817.

[Olhoeft, 1989] Olhoeft, G. R. (1989). *Physical Properties of Rocks and Minerals*, chapter Electrical properties of rocks, pages 257–330. Taylor and Francis, Philadelphia, Pa.

[Pettinelli et al., 2003] Pettinelli, E., Burghignoli, P., Galli, A., Pisani, A. R., Ticconi, F., DelVento, D., and Cereti, A. (2003). Electromagnetic propagation modelling for GPR exploration of Martian subsoil. In *Third Mars Polar Science Conference*.

[Prager, 1961] Prager, S. (1961). Viscous flow through porous media. *The Physics of Fluids*, 4(12):1477–1482.

[Taflove and Hagness, 2000] Taflove, A. and Hagness, S. C. (2000). *Computational Electrodynamics: the finite-difference time-domain method, 2nd edition*. Artech House,Inc.

[Tsang et al., 2000] Tsang, L., Kong, J. A., and Ding, K. (2000). *Scattering of electromagnetic waves: Theories and applications*, chapter Characteristics of discrete scatterers and rough surfaces, pages 167–197. John Wiley and Sons, Inc.

[Ulaby et al., 1982] Ulaby, F. T., Moore, R. K., and Fung, A. K. (1982). *Microwave Remote Sensing: active and passive VOL II*, chapter Physical mechanisms and empirical models for scattering and emission, pages 816–853. Addison-Wesley Publishing Company.

[Yee, 1966] Yee, K. S. (1966). Numerical solution of initial boundary value problems involving maxwell's equations in isotropic media. *IEEE Transaction on Antennas and Propagation*.